npj Natural Hazards

https://doi.org/10.1038/s44304-026-00214-7

Article in Press

The ash concentration of co-PDC clouds: implications for operational modelling and the aviation hazard

Received: 10 December 2025

Accepted: 19 April 2026

Cite this article as: Hagenbourger, M., Jones, T.J., Beckett, F.M. *et al.* The ash concentration of co-PDC clouds: implications for operational modelling and the aviation hazard. *npj Nat. Hazards* (2026). https://doi.org/10.1038/s44304-026-00214-7

Marie Hagenbourger, Thomas J. Jones, Frances M. Beckett & Samantha L. Engwell

npj Natural Hazards

'The ash concentration of co-PDC clouds: implications for operational modelling and the aviation hazard'

Marie Hagenbourger[1*], Thomas J. Jones[1], Frances M. Beckett[2], and Samantha L. Engwell[3]

[1] *Lancaster Environment Centre, Lancaster University, Lancaster, United Kingdom*
[2] *Met Office, Exeter, United Kingdom*
[3] *British Geological Survey, The Lyell Centre, Edinburgh, United Kingdom*
[*] *Corresponding authors. Email: m.hagenbourger@lancaster.ac.uk*

Pyroclastic density currents (PDCs) can generate co-PDC plumes, which segregate and buoyantly rise from the underlying gravity current. Using the atmospheric-dispersion model NAME we perform a series of co-PDC simulations that vary the particle release height and mass eruption rate for eight different weather patterns that characterise the UK and the surrounding European area. We examine the ash cloud concentration as a function of vertical elevation (flight level) within the atmosphere. We find that the ash clouds are compact in shape and often contain high (above $10\,\mathrm{mg\,m^{-3}}$) ash concentrations in the first few hours after particle release. Our results are discussed in terms of the hazard to aviation and operational modelling by volcanic ash advisory centres.

Introduction

Fast-moving volcanic gravity currents, termed pyroclastic density currents (PDCs), can be formed by the collapse of an eruption column[1–8], from collapse of lava domes or flow fronts[9–15]. The generated mixtures are multiphase and comprise both hot gas and solid particles, e.g., volcanic ash, lithic fragments. Accompanying plumes, commonly termed co-PDCs, and also known as phoenix clouds or co-ignimbrites[15–22], can form from PDCs by air entrainment. The upper part of the PDC buoyantly lifts off and forms the co-PDC[18,19,21,23–25]. Therefore, co-PDCs are composed of hot gas and fine particles (the heavier particles remain in the denser, ground-hugging current). The co-PDC plumes rise until they reach a level of neutral buoyancy in the atmosphere and then disperse laterally. Given these formation conditions, co-PDCs have some unique eruption source parameters (ESPs) compared to typical vent-derived plumes, for example, co-PDCs have been found to have fine particle sizes ($< 90\,\mu m$)[15,18] and a high-aspect ratio source geometry (i.e., irregular shaped, not a circular or point-source). Co-PDCs can be generated from the entire length of the underlying PDC or from a discrete part[18] and thus do not necessarily form at the vent. Co-PDCs have the potential to occur during any explosive eruption, and their formation processes and associated ash dispersion have been observed in several historic eruptions[18]. Despite this prevalence, little work has been done on forecasting the presence and dispersal of co-PDC ash in the atmosphere.

Volcanic ash can have a significant impact on infrastructure, human health, livestock, soil fertility, and crops[2,18,26]. Ash also represents a significant hazard to aviation[27–37], with a key example being the 2010 Eyjafjallajökull eruption, which dispersed ash over Europe, leading to an approximate US$ 2 billion loss for the aviation industry[29]. Volcanic ash (i.e., particles $\leq 2\,mm$) travel long distances, and disperse over wide areas[27,38]. Therefore, aircraft are not only exposed to hazard from volcanic ash close to the eruptive source, but many thousands of kilometres downwind. High ash concentrations can lead to aircraft damage, as ash entering the engines may be heated to above their glass transition temperatures[39]. This can create engine disturbance by clogging air bleed holes or sticking to surfaces[29,35,37,40] and damage thermal barrier coatings[41–43]. Ash ingestion can also cause malfunction of electronic components or pressure losses[29,40]. Examples of impacted electronic components include speed indicators, pressure sensors, engine power, and interference with communication and navigation systems. Ash also has abrasive effects, especially on the leading edges, fan blades, or on the windshields, and this damage may only be visible after long-term exposure[29,35,37,40,44,45].

Volcanic Ash Advisory Centers (VAAC) are responsible for providing ash hazard information to civil aviation. For the aviation industry to mitigate against the ash hazard and retain flight safety, they need to know the location of the ash cloud in the atmosphere and its ash concentration. VAACs communicate this hazard through the issuance of volcanic ash advisories[46]. In November 2025, VAACs started to issue Quantitative Volcanic Ash (QVA) information. QVA forecasts contain

ranges and thresholds of ash concentration. 'Low' concentrations are defined as ash concentrations within the range 0.2-2 mg m^{-3}. 'Medium' concentration is defined as 2-5 mg m^{-3} and 'high' ash concentration is 5-10 mg m^{-3}, while ash concentrations of $\geq$ 10 mg m^{-3} are classified as 'very high'[47]. The minimum satellite detection threshold of ash particles is approximately 0.2 g m^{-2} total column mass loading[29,47–50].

The International Civil Aviation Organisation (ICAO) has standard regulations on flight levels (abbreviated as FL) to provide adequate vertical separation between aircraft and sufficient terrain clearance[51]. FLs are parallel surface levels of constant atmospheric pressure, with reference to a pressure datum, FL 0, which is 1013.2 hPa (1013.2 millibars) in the 'ICAO Standard Atmosphere'[51,52], and equivalent to mean sea level. The relationship between flight level, atmospheric pressure, and weather is shown schematically in Figure 1. Meteorological conditions impact the altitude (above

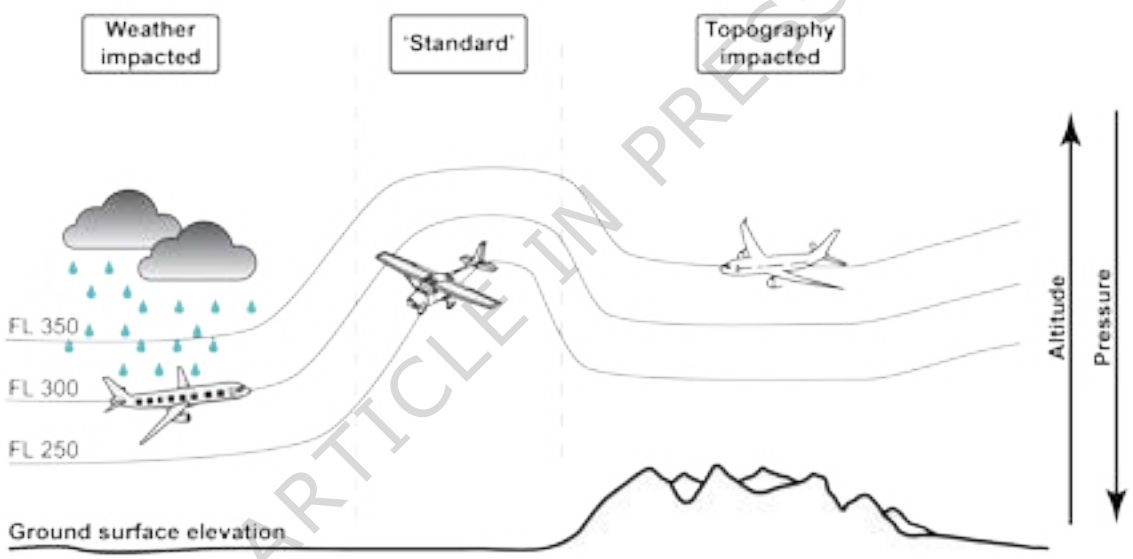

Figure 1: Flight levels (FL) retain vertical separation despite atmospheric pressure variations due to different weather conditions and large changes in ground topography. The 'standard' region, shown in the middle of the figure, is shown as a reference. Despite the cruise flight level being fixed (e.g., FL 300), the aircraft changes its actual altitude (i.e., km above sea level) during flight.

sea level) of the flight levels, for example, precipitation, often caused by a depression, lowers the atmospheric pressure and therefore the altitude of the corresponding FL. Similarly, the atmospheric pressure can be impacted by changes in the topography.

Commercial aircraft typically fly at a cruising altitude just below the tropopause[29] between 8.8-12.5 km above sea level (asl)[53], corresponding to approximately FL290 to FL410 at standard

atmospheric pressure. Such flights follow a set of well-defined flight phases: taxi, take-off, en-route (climb, cruise, and descent), approach, and landing[54]. A plane's altimeter specifies the current flight altitude, and the altimeter scale corresponds to a particular barometric pressure at a certain location and time[51]. During take-off, landing, and below a certain transition altitude (a specific altitude above a minimum distance from the ground or aerodrome[51]), commonly at 457 m (1500 ft), planes set their altimeter to the current air pressure of the airport or the applied location. However, at higher altitudes (above the specific transition altitude and when in cruise flight), a standard reference set of 'flight levels' is used, and flying heights are determined based on pressure. This ensures that every plane uses the same reference for altitude determination for consistency. Planes do not fly at a constant altitude above the ground but rather follow an assigned flight level. For this reason, volcanic ash concentrations in the atmosphere, and forecast model outputs are commonly reported per FL, conforming to regulatory (i.e., QVA) requirements.

The UK Met Office's Numerical Atmospheric-dispersion Modelling Environment (NAME) models particle transport and dispersion in the atmosphere by releasing a large number of model particles into a model environment. Simulations are then driven using pre-processed global atmospheric conditions from the Met Office's Unified Model (MetUM)[55,56], a Numerical Weather Prediction model (NWP). NAME is used by the London VAAC as its operational model for volcanic ash forecasts. Our research uses the NAME model with output results as a function of FL. The vertical resolution of both the wind vector (ρ) and temperature (θ) data reduce with height, respectively (Figure 2). For altitudes corresponding to where commercial planes fly and the maximum FL requested by QVA (at standard atmospheric pressure: FL600), at least two ρ and θ datasets are available for each FL (at standard pressure). Whereas at altitudes $>\approx 25$ km asl these meteorological datasets (ρ and θ) have a vertical spacing greater than one FL, and as such, meteorological data availability is limited.

A few studies have modelled co-PDC rise, transport, and dispersion[14,21–23,25,57–61]. Of most relevance here Hagenbourger *et al.*[57] used NAME to study the sensitivity of total column mass loadings to the unique eruption source parameters (ESPs), i.e., the source area and aspect ratio, associated with co-PDCs. However, little is known about the vertical concentration of ash (in mg m^{-3}) in a dispersing co-PDC cloud – which is critical for assessing the aviation hazard. While numerous publications discuss the vertical distribution of ash in vent-derived ash clouds (e.g.[19,24,62–64]), no such studies specifically focus on co-PDCs. Furthermore, given the unique ESPs of co-PDCs, limited insight can be gained from our knowledge of vent-derived plumes.

Here, we bridge this gap by (1) performing a series of NAME model runs for co-PDC ash dispersion and transport, (2) analysing the resultant atmospheric ash concentrations in the vertical (i.e., at different FLs) and (3) discussing whether the concentration could have a meaningful impact on aviation. Here, the term 'cloud' is used to refer to downwind ash transport and dispersion, while the term 'plume' solely describes the near-source behaviour.

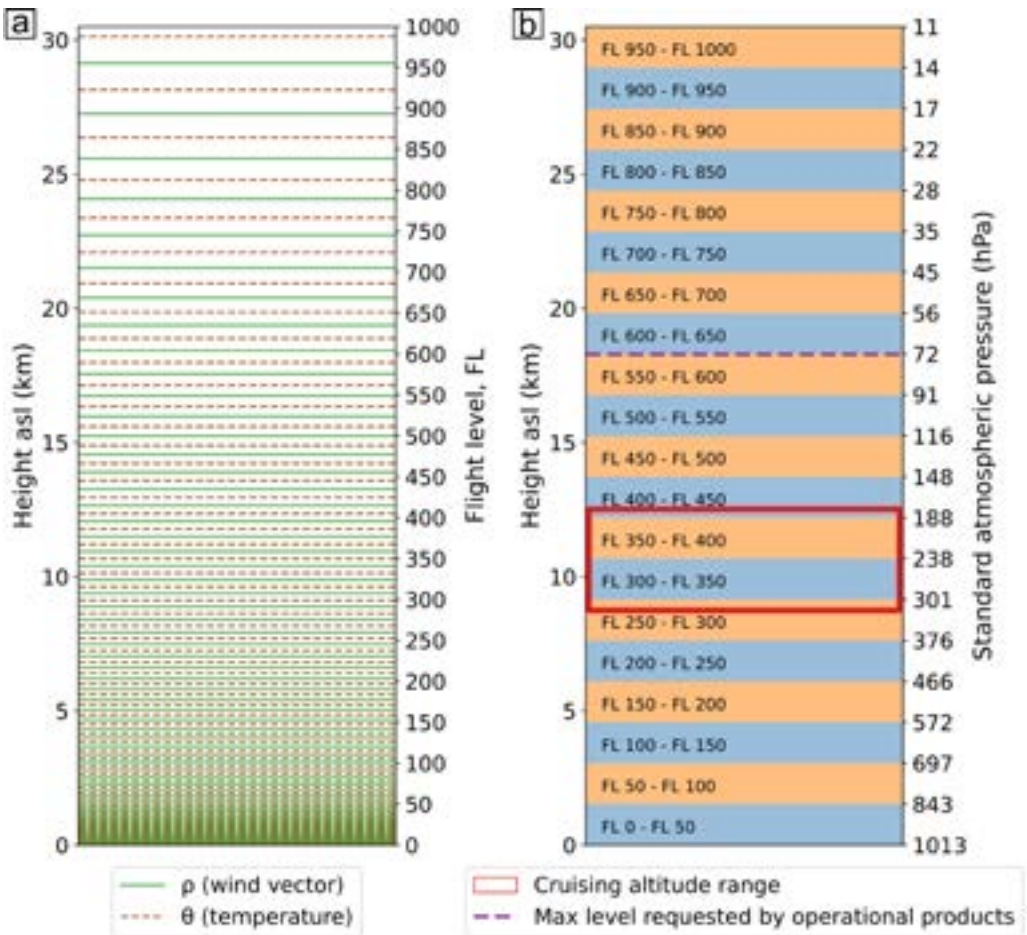

Figure 2: The vertical resolution of the Met Office Unified Model (MetUM) compared with flight level, FL. **(a)** 'ρ' and 'θ' levels contain the wind vector data and the temperature data, respectively. The vertical resolution of both data sets decreases with increasing height above sea level (asl). **(b)** NAME outputs FL in steps of 50 in this study. Despite FL being pressure-based, the standard atmosphere pressure curve is used for comparison (1013.2 hPa $\equiv$ FL0). The purple dashed line indicates the maximum FL (FL600) requested by aviation for QVA analysis.

Methods

Modelling and NAME setup

NAME can be used to predict atmospheric transport, dispersion, and deposition of gases and particles[65]. It uses the advection-diffusion equation and outputs the concentration of particles. Here, NAME III (v8.6)[55,65] was used in the Lagrangian configuration to model the ash transport and

dispersion of a volcanic ash cloud derived from a co-PDC plume. We used the NAME wet and dry deposition schemes[32,66–68] and assumed ESP time homogeneity. This is an idealisation for modelling purposes, and we are aware that PDCs and co-PDCs are not constant in time (e.g., the 1980 Mount St. Helens eruption, USA[69,70] (hereafter MSH), and the 2015 Calbuco eruption, Chile[71]).

We used the pressure-as-height coordinate system to relate the height, z_{ICAO}, to the ICAO standard atmosphere pressure. Adapted from NAME[65] this is expressed as:

$$z_{ICAO} = \begin{cases} \dfrac{T_{msl}}{\gamma_{0-11}} \left(1 - \left(\dfrac{p}{p_{msl}} \right)^{\frac{R\gamma_{0-11}}{g}} \right) & \text{for} \quad p \geq p_{11} \\ z_{11} + \dfrac{RT_{11}}{g} \ln \left(\dfrac{p_{11}}{p} \right) & \text{for} \quad p_{11} > p > p_{20} \\ z_{20} + \dfrac{T_{20}}{\gamma_{20+}} \left(1 - \left(\dfrac{p}{p_{20}} \right)^{\frac{R\gamma_{20+}}{g}} \right) & \text{for} \quad p \leq p_{20} \end{cases} \tag{1}$$

with

$$p_{11} = p_{msl} \left(1 - \frac{\gamma_{0-11}}{T_{msl}} z_{11} \right)^{\frac{g}{R\gamma}} \tag{2}$$

$$p_{20} = p_{11} \exp \left(-\frac{g}{RT_{11}} (z_{20} - z_{11}) \right) \tag{3}$$

where R is the specific gas constant for dry air, $R = 287.05\,\mathrm{J\,kg^{-1}\,K^{-1}}$; T_{msl} is the temperature at mean sea level (msl), $T_{msl} = 288.15\,\mathrm{K}$; T_{11} is the temperature at 11 km asl, $T_{11} = 216.65\,\mathrm{K}$; T_{20} is the temperature at 20 km asl, $T_{20} = 216.65\,\mathrm{K}$; γ_{0-11} is the lapse rate from 0-11 km asl, $\gamma_{0-11} = 0.0065\,\mathrm{K\,m^{-1}}$ and γ_{20+} is the lapse rate at altitudes greater than 20 km asl, $\gamma_{20+} = -0.001\,\mathrm{K\,m^{-1}}$. As in the ICAO standard atmosphere, the lapse rate is assumed to be constant between specified altitudes[72]. p_{msl} is the standard pressure at msl, $p_{msl} = 101\,325\,\mathrm{Pa}$; z_{11} stands for the altitude of 11 km above msl, when using the hydrostatic assumption; p_{11} corresponds to the pressure at z_{11}.

The applied meteorological data archive uses interpolated meteorological data in time and space (when using the Lagrangian approach)[32]. For the eruption setup, we used a pre-processed, configured NWP dataset from the Global configuration of the MetUM[55,56,73,74]. The meteorology definition applied here has a global horizontal resolution with grid lengths of approximately 10 km at mid-latitudes. The computational grid in NAME has a horizontal grid resolution of 0.1° in Latitude and Longitude, and throughout the model domain, the vertical grid resolution decreases with vertical height (Figure 2). The vertical ash concentration was output over vertical depths of 5000 ft (approximately 1500 m), which corresponds to a depth of 50 FL (at standard atmospheric pressure; Figure 2).

Weather patterns group characteristic recurring circulation types, i.e. similar weather occurrences

over a defined region. The prevalent weather pattern over the specific region can vary daily. Neal *et al.*[75] defined a set of eight weather patterns for the North Atlantic and European region (30° W – 20° E and 35° – 70° N), which are used for seasonal and long-range forecasts and for identifying key changes in wind flow[75]. These eight weather patterns, illustrated in Figure S1, are numbered in order of the annual historical occurrence between 1850 and 2003. The lower numbers indicate a greater frequency, i.e., over the whole year, weather pattern 1 occurs more often than weather pattern 8. For a full description the reader is referred to Neal *et al.*[75].

We used these weather patterns to consider the impact of meteorology on our results. We did not perform a climatology study, but used weather patterns to better underpin and confirm that our findings are not exclusively based on one sampled day. For each weather pattern, three different days from different seasons were manually selected for model runs. In total, we performed model runs across 24 days (Table S1), and the distribution of these days is presented in Figure S2.

Each of these 24 days has been run for particle emission start times of 06:00 UTC, 14:00 UTC and 22:00 UTC for a forecast duration of 36 h (288 runs in total). Additionally, for 31st January 2022, we also ran at a fourth time of 09:00 UTC in order to compare with the previous co-PDC study in Hagenbourger *et al.*[57]. The different start times were chosen by considering the diurnal cycle and the atmospheric boundary layer. The diurnal cycle refers to a daily cycle of weather changes (i.e., temperature fluctuations), and the atmospheric boundary layer (i.e., the layer between the planetary surface and free atmosphere) depends on the temperature of the ground. The lowest temperature occurs close to sunrise, between 6-7 am local time, while the maximum occurs at 2-3 pm local time[76,77]. The time difference between the extremes is about ~ 8 h, which aligns to 8 h spacing in our run start times.

Eruption conditions

This study used a 10 min particle release or emission time, t_r, which corresponds to observations of large co-PDC plumes[69]. Model particles were released into the atmosphere at the level of neutral buoyancy, z, over a defined thickness, dz. This thickness of the release around z is given by the ratio of the total column height, H_T, defined as[78–81]:

$$dz = 0.3 \cdot H_T \ . \tag{4}$$

Here, we approximate dz as ranging from $0.7 \cdot H_T$ to H_T while neglecting any overshooting top. The May 18th 1980 eruption of MSH is the largest observed and well-documented co-PDC in the literature. Therefore, in this work, we used parameter values (i.e., A, α, dx, dy, t_r; refer to Table 1) related to this eruption. As it represents one of the largest co-PDC plumes, any reported ash concentrations and cloud footprints represent a reasonable upper limit. Exceeding these parameters, although possible, is rarely observed in nature, and such events might be governed by different

physical processes. Hagenbourger *et al.*[57] showed that the particle release height significantly affects the horizontal ash cloud transport, whereas the effects of source area and source aspect ratio are negligible. Following this study, here, we consider the vertical downwind concentrations of volcanic ash from a co-PDC release and its sensitivity to plume height and mass eruption rate (MER). The particles were assumed to be spherical with a total grain size distribution (TGSD) as in Hagenbourger *et al.*[57] with a modal grain size in the grain size range of 26-74 µm. We applied the entire TGSD and no distal fine ash fraction as the entire distribution is relatively fine (i.e., 86% < 105 µm). Hekla volcano in Iceland (63.98° N, 19.67° W)[82] was used as the source location; however, the source location is not unique for our study, as we are not studying local topographic influences or volcano properties. We selected Hekla for its distance of 51 km to the Atlantic Ocean, so that the entire source area of the co-PDC remained on land.

Table 1: Co-PDC source parameters used in this study. A, α, dx, dy, P and t_r refer to the May 18$^{\text{th}}$ 1980 eruption of MSH[57]. See Hagenbourger *et al.*[57] for references to H_T and dz. t_r has been taken from Sparks *et al.*[69].

Parameter	Symbol	Unit	Value(s)
Release Area	A	km^2	619
Aspect ratio	α	-	1.7
Width of source in plan view	dx	km	32.4
Length of source in plan view	dy	km	19.1
Source perimeter	P	km	103.0
Maximum plume height	H_T	km	15, 20, 25 & 27
Thickness of ash release	dz	km	4.5, 6.0, 7.5 & 8.1
Particle emission time	t_r	min	10
Particle density	ρ	kg m^{-3}	2500

The total height of co-PDC plumes has been observed[57] in nature in the range of 1-30 km. Traditionally, H_T is coupled to the MER by an empirical power law[80,81,83–85]. Here, we used the MER–H_T-relationship from Aubry *et al.*[83]:

$$\text{MER} = \sqrt[0.226]{\frac{H_T}{0.345}} \,. \tag{5}$$

The H_T and MER of MSH fall within the confidence interval of this relationship in Equation 5, thus applicable here, for our modelled co-PDC plumes, and used in the absence of any other specific MER–H_T-relationship for co-PDCs. Data for very small co-PDC are not included in this relationship, we therefore limit our modelled range of H_T to 15 km, 20 km, 25 km, and 27 km. The aspect ratio, α, of the particle release area/source was set as a constant parameter describing the relationship of the source area's width by length (dx/dy) to be 1.7 (Table 1; Hagenbourger *et al.*[57]).

Numerical Experiment

The volcanic ash cloud was simulated for 36 h with data output every 1 h. Table 2 defines all parameters and their variation for our set of model runs, or 'numerical experiment'. The different values of H_T define unique values of dz and MER, following Equation 4 and Equation 5, respectively. We used a particle density of 2500 kg m^{-3} and assumed no particle aggregation. All other eruption source parameters used in this study were kept constant, as defined in Table 1. The numerical experiment was then repeated for different weather patterns and dates (Figure S2).

Table 2: Source parameters used in the numerical experiment. Four release heights, H_T, were each used for three release start times. The range of covered flight levels of the release region is indicated and rounded to the nearest ten.

Tot. plume height, H_T (km agl)	dz (km)	FL range of release region	MER (kg s^{-1})	Calculated released mass into atmosphere (kg)	Calculated released volume (m^3)	Release start time (UTC)		
15	4.5	270 - 420	1.77×10^7	1.06×10^{10}	4.26×10^6	06:00	14:00	22:00
20	6.0	360 - 560	6.34×10^7	3.80×10^{10}	1.52×10^7			
25	7.5	450 - 670	1.70×10^8	1.02×10^{11}	4.08×10^7			
27	8.1	490 - 750	2.39×10^8	1.43×10^{11}	5.74×10^7			

The specific model run with a $H_T = 27$ km, corresponding[83] to MER $= 2.39 \times 10^8$ kg s^{-1}, yields a total mass release of 1.43×10^{11} kg for $t_r = 10$ min. This is consistent with published literature[69,84] on MSH and thus supports our selection of source parameters. Furthermore, all our models runs can be classified as a VEI 2 on the Volcanic Explosivity Index (VEI) scale[86]. Although our plume heights are high, the released volumes from co-PDCs are small due to the short t_r.

Results

We focus on the impacts on the dispersed downwind cloud in terms of its location, area, concentration (with reference to QVA), and vertical mass distribution. All these results are reported across a range of weather patterns, H_T and MERs.

Figure 3 provides an illustrative example of how concentrations at specific vertical intervals (i.e., at specific FLs) relate to commonly reported total column mass loadings. The total column mass loadings (g m^{-2}), shown in Figure 3a, are the total integrated mass through the entire vertical column. Figure 3b - l represent the ash concentration (mg m^{-3}) within different altitude layers (i.e.,

at different flight levels). The maximum extent of the ash cloud with total column mass loadings $\geq 0.2\,\mathrm{g\,m^{-2}}$, constrains the total horizontal footprint. The regions of ash located within each FL vary in size, shape, location, and ash concentration (Figure 3b - l), but sum to provide the total column mass loading (Figure 3a). In this example, at the highest FLs, the cloud area is relatively small, whereas for the middle FLs (i.e., FL300 - FL600), the cloud varies in size and is typically more elongated in shape. The shape, area, and concentration also depend on the time since particle release.

Ash cloud location

The North Atlantic and European region can be characterised by eight weather patterns[75] which group similar weather occurrences over a defined region. We now evaluate if the ash cloud location systemically varies between each weather pattern (Figure 4). We have chosen to display $H_T = 27\,\mathrm{km}$ because the most (vertical) diversity was shown; however, the trends described in this section remain true for all the different flight levels. Our full dataset can be found in the supplementary information (Figure S3 displays FL300 - FL350 and Figure S4 displays FL900 - FL950).

Across all of the eight weather patterns, we found that the ash clouds (Figure 4; all at 12 h since particle release at FL550 - FL600) were remarkably discrete and isolated; they feature a highly concentrated region, with very minor lower concentration margins. Throughout the whole range of weather patterns at FL550 - FL600, QVA classification declares the ash concentration as 'very high' ($\geq 10\,\mathrm{mg\,m^{-3}}$), as seen by the dark red coloured ash clouds in the outputs. Also, the cloud trajectories were mainly towards Europe for all runs and weather patterns. However, even within the same weather pattern at the same period of time after the particle release, the specific location of the ash cloud is highly variable, and both the cloud shape and size often show large variability.

The three ash transport and dispersion outputs corresponding to weather pattern 1 (Figure 4a) are all located in different positions – there is no spatial overlap between the outputs. Two of the ash clouds are located relatively close to Iceland, while the other ash cloud is elongated and stretched close to the north coasts of Scotland and Norway. For weather pattern 2 (Figure 4b), one cloud is highly elongated while the other two are more compact and remain closer to the source. Outputs for weather pattern 3 (Figure 4c) are widely spread in terms of location; however, they exhibit a similar plume shape. In general, all of the outputs for weather pattern 4 (Figure 4d) are elongated; however, like the outputs from weather pattern 3, they are widely spread in terms of location while considering the same point in time. Ash concentrations from weather patterns 5 and 6 (Figure 4e & f) both show two ash clouds located directly over the Icelandic land mass, while the third is located in the Arctic Ocean and the Atlantic Ocean, respectively. For weather patterns 7 and 8 (Figure 4g & h), the outputs illustrate that the ash clouds have not travelled far from the source within 12 h.

Figure 5 compares the ash concentration (in $\mathrm{mg\,m^{-3}}$) as a function of H_T for a specific flight

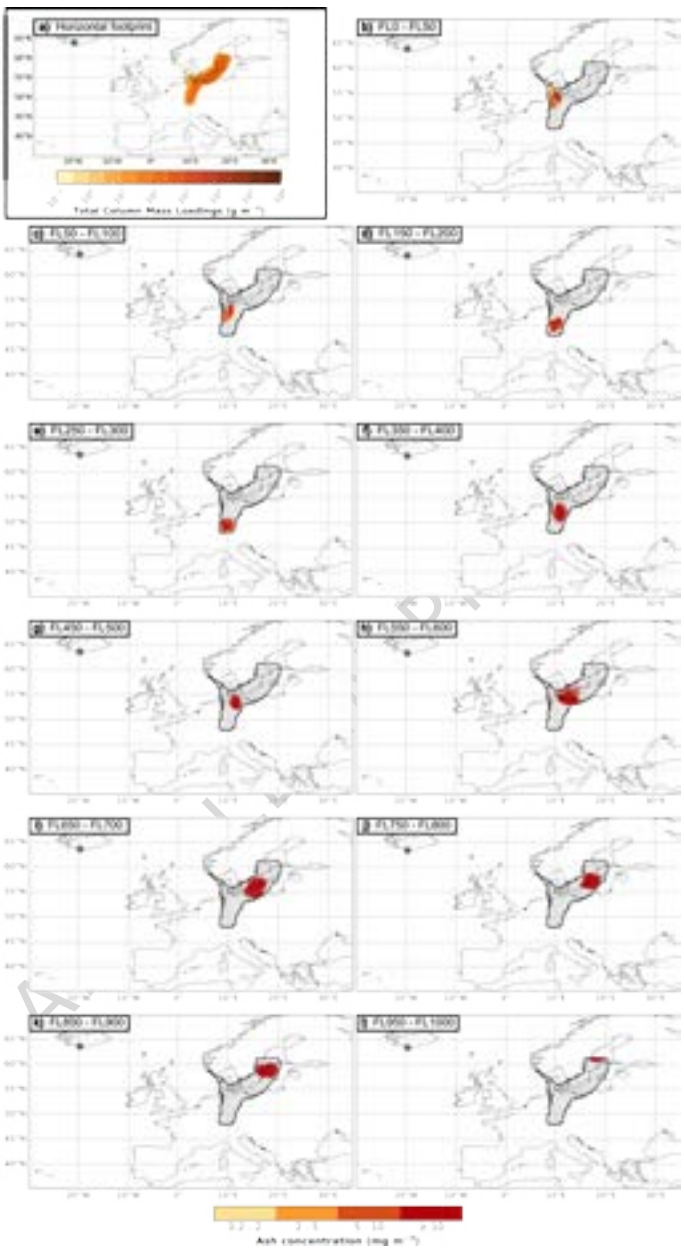

Figure 3: Illustration of the relationship between **(a)** the horizontal footprint of total column mass loadings ($\mathrm{g\,m^{-2}}$) and **(b-l)** the vertical output shown at selected flight levels (in $\mathrm{mg\,m^{-3}}$) at 12 h after the particle release. The black outline in (b - l) represents the boundary of total column mass loadings $\geq 0.2\,\mathrm{g\,m^{-2}}$. Particles were released at $H_T = 27$ km on 31$^{\mathrm{st}}$ Jan 2022 at 14:00 UTC. In all panels, a blue star indicates the release location. Note the difference in the range and the units of the colour bars between the total column (a) and vertical outputs b - l).

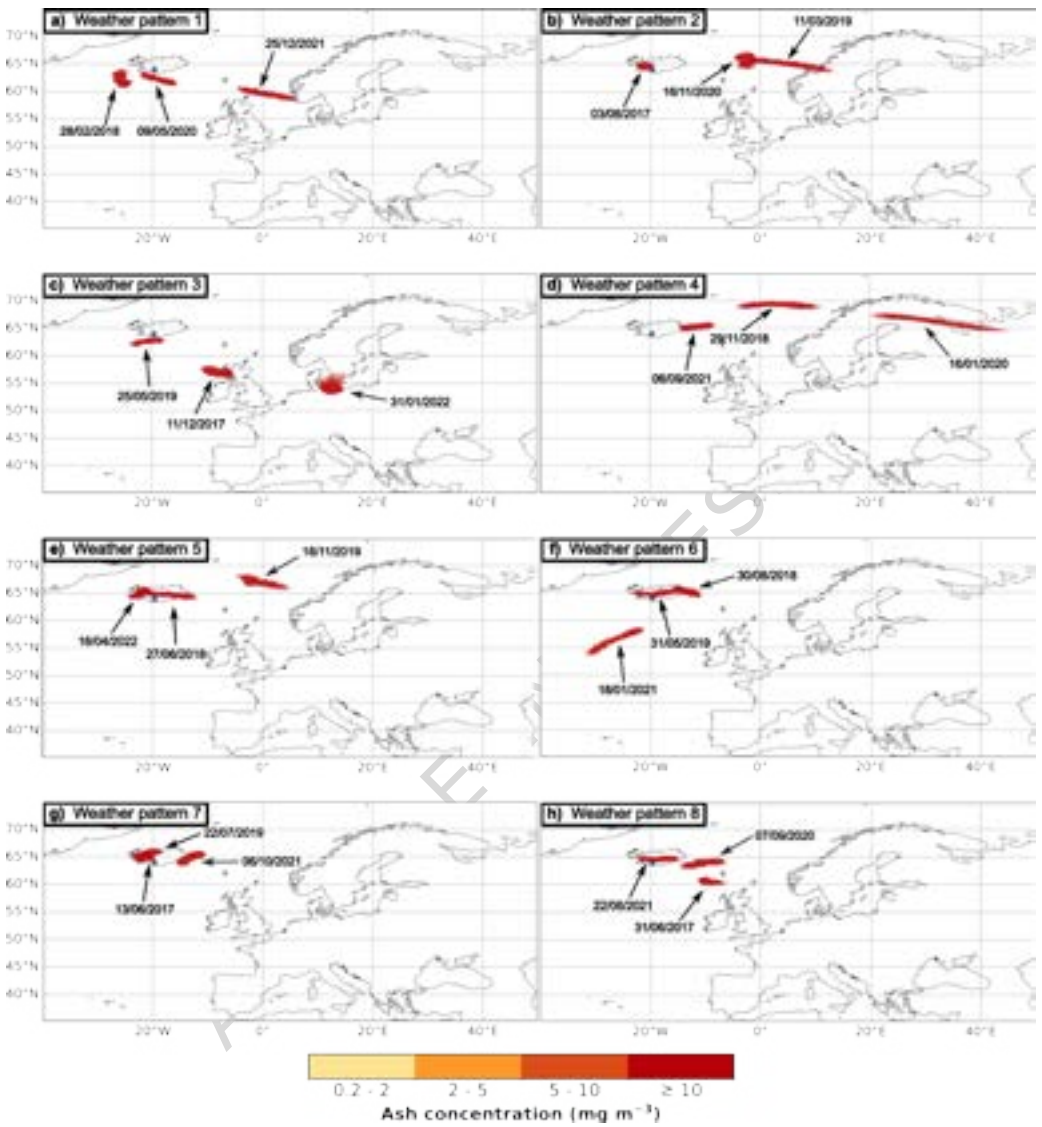

Figure 4: Ash cloud location displayed for the eight weather patterns at 12 h after particles were released at $H_T = 27$ km at 14:00 UTC. FL550 - FL600 is displayed for all. Each subfigure contains three separate NAME model outputs, and thus displays three different ash clouds generated for each weather pattern. These are indicated by the black arrows, and the dates correspond to the associated eruption/release start. Some of the ash clouds within a weather pattern slightly overlap in this figure. In all panels, a blue star indicates the release location, and the data are given as ash concentration in mg m^{-3}.

level (here, FL300 - FL350, where commercial planes fly), and a specific weather pattern (here, number 3). For a given day, the ash cloud locations are similar for all release heights (H_T = 15 km, 20 km, 25 km and 27 km), simply highlighting how the ash cloud dispersal is highly sensitive to the specific meteorological conditions. However, the cloud extent, ash concentration, and shape differ as a function of H_T. Ash released at H_T = 25 km and H_T = 27 km (Figure 5c & d) show similar behaviour in terms of their location, size, concentration, and shape. H_T = 15 km (Figure 5a) contains mainly low to medium ash concentrations (yellow and orange colours), whereas very high ash concentrations are present in both H_T = 25 km and H_T = 27 km (Figure 5c & d) (dark red, $\geq 10\,\mathrm{mg\,m^{-3}}$). The location of the ash cloud at the higher FLs (e.g., FL550 - FL600 and FL900 - FL950) does not change significantly when H_T is varied (Figure S5 and Figure S6, respectively). However, the ash cloud location within lower FLs is more sensitive to H_T (Figure 5).

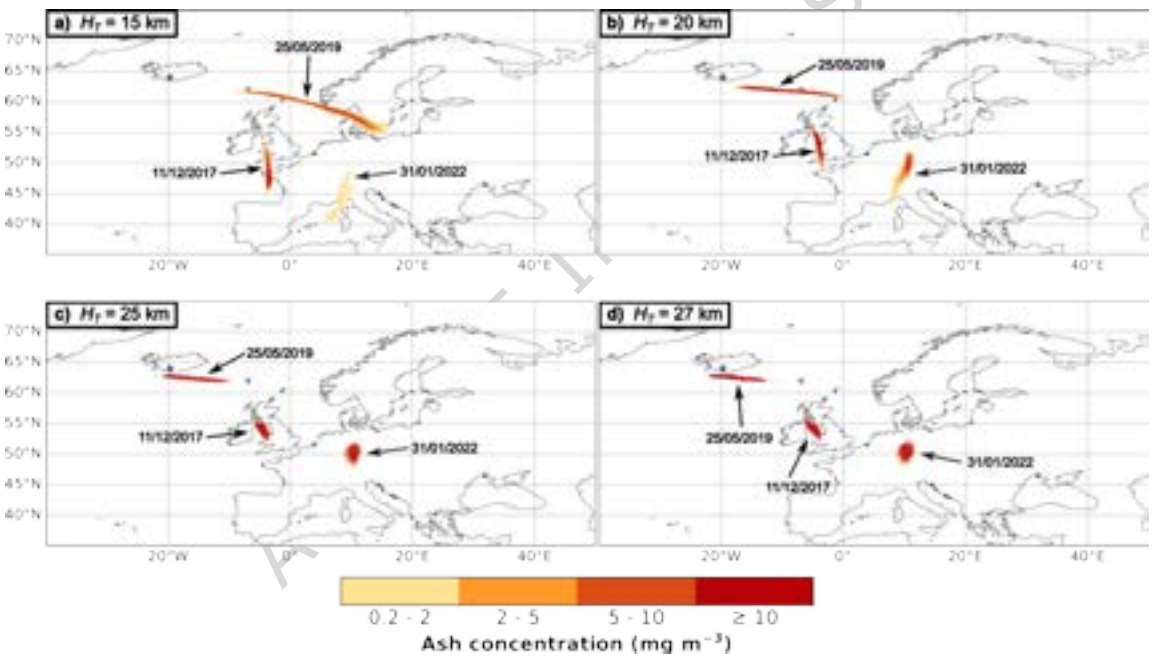

Figure 5: Ash cloud locations for particle release heights of **(a)** H_T = 15 km, **(b)** H_T = 20 km, **(c)** H_T = 25 km, and **(d)** H_T = 27 km for weather pattern number 3 at 12 h since particle release start time. The particles were released on 31st Jan 2022 at 14:00 UTC. Each subfigure shows three different model run outputs at FL300 - FL350 for different dates. In all panels, a blue star indicates the release location, and the data are given as ash concentration in $\mathrm{mg\,m^{-3}}$.

Ash cloud area at each Flight Level

The total area of the downwind ash cloud is reported as a function of time for each H_T with ash concentrations $\geq 0.2\,\mathrm{mg\,m^{-3}}$ (Figure 6). We chose the same date (31$^{\mathrm{st}}$ January 2022, 14:00 UTC) as was used to illustrate the ash cloud behaviour(Figure 3). For all values of H_T, divergence in total ash cloud area is observed with time. The areal extent of the cloud spreads noticeably from the time of release and shows little particle deposition, i.e., no large reductions in cloud area within the first 36 h. $H_T = 15\,\mathrm{km}$ (Figure 6a) generates an ash cloud reaching FLs up to approximately FL600; $H_T = 20\,\mathrm{km}$ generates a cloud up to FL800 (purple coloured lines), $H_T = 25\,\mathrm{km}$ reaches up to FL950, while $H_T = 27\,\mathrm{km}$ covers the full FL range investigated here, up to FL1000. Figure 6c and Figure 6d, corresponding to $H_T = 25\,\mathrm{km}$ and $H_T = 27\,\mathrm{km}$, respectively, show similar cloud area distributions across the different flight levels. Across all release heights, the range of FL250 - FL500, corresponding to the orange, yellow, and green lines in Figure 6, is among the largest cloud areas for all time steps analysed. Furthermore, although the absolute magnitude of these co-PDC ash cloud areas is relatively small ($\sim 300.000\,\mathrm{km^2}$), the main altitude range they occupy corresponds to flight levels used for commercial aircraft (FL300 - FL400).

We can also analyse the ash cloud area corresponding to each of the different QVA thresholds. As an illustrative example, Figure 7 shows the ash cloud areas within the QVA threshold ranges for $H_T = 27\,\mathrm{km}$ and particle release on 31$^{\mathrm{st}}$ January 2022, 14:00 UTC. For completeness, all the other release heights are provided in the supplementary information (Figures S5-S7). This analysis confirms that for $H_T = 27\,\mathrm{km}$ and $H_T = 25\,\mathrm{km}$ the generated clouds have mostly 'high' (5-10 $\mathrm{mg\,m^{-3}}$) to 'very high' ($\geq 10\,\mathrm{mg\,m^{-3}}$) ash concentrations across the entire set of FLs, and FLs $\geq$ FL500 only contain ash concentrations $\geq 5\,\mathrm{mg\,m^{-3}}$ (Figure 7c & d and Figure S9c & d). Furthermore, for $H_T \geq 20\,\mathrm{km}$, most of the cloud area corresponding to the 0.2-2 $\mathrm{mg\,m^{-3}}$ concentration range is located near to the ground level (pink and orange coloured lines), which reflects particle settling (Figure S8d, Figure S9d and Figure 7d). In contrast, for $H_T = 15\,\mathrm{km}$, the lowest H_T studied, most of the cloud contains lower ash concentrations 0.2-2 $\mathrm{mg\,m^{-3}}$ (Figure S7a), and ash concentrations with $\geq 10\,\mathrm{mg\,m^{-3}}$ are not present in most FLs after 27 h since particle release (Figure S7d). However, FL350 - FL450 (covering commercial airspace use) are still impacted by 'very high' ash concentrations throughout the 34 h modelled for.

Vertical location of the maximum mass

It is also important for aviation to consider where the dispersed ash resides in terms of mass. Here, this is done by reporting the vertical location where (i) the maximum amount of ash is located and (ii) the highest FL that the ash reaches for concentrations $\geq 0.2\,\mathrm{mg\,m^{-3}}$. The minimum ash cloud height is simply taken as ground level, as ash settles from the cloud. For all start times across all weather patterns, the maximum FL achieved by the co-PDC ash is always situated above the release

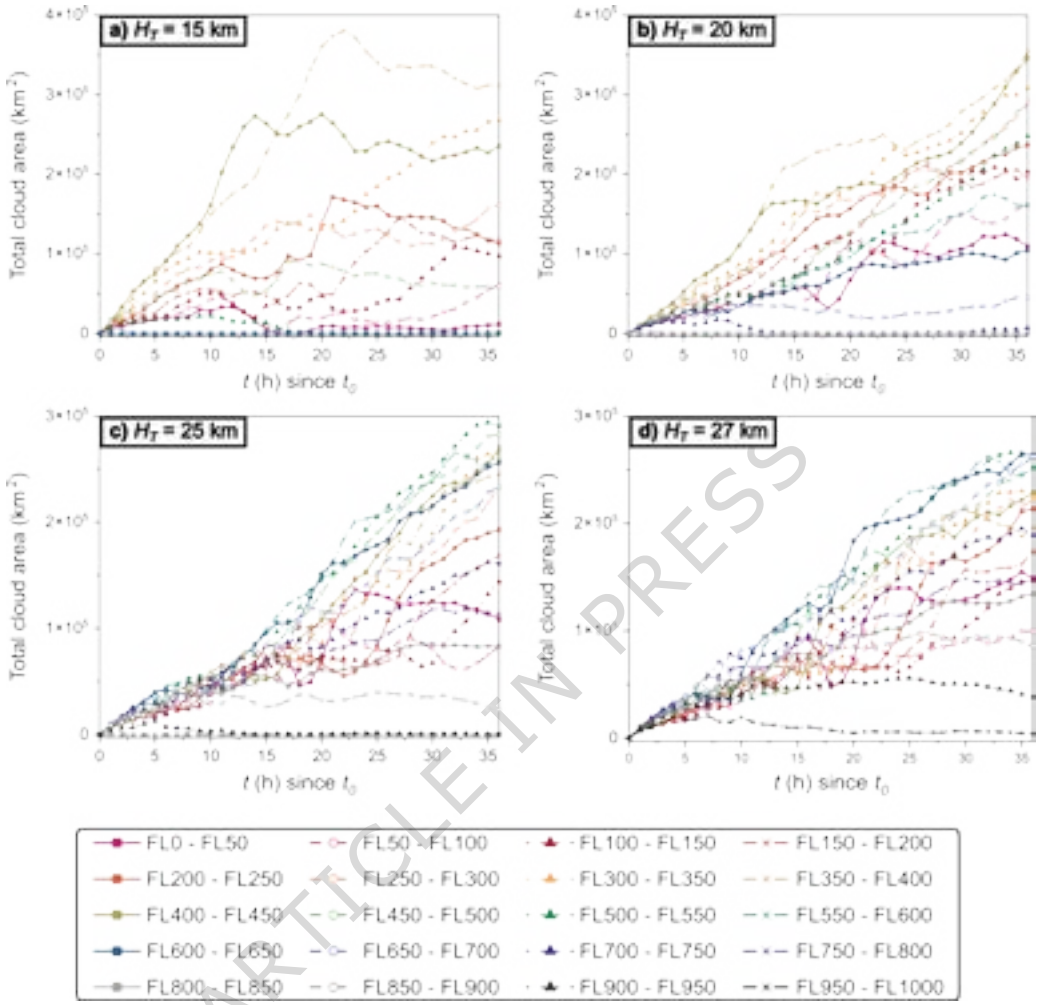

Figure 6: Total ash cloud area at each 50 FL as a function of time for particle release heights of **(a)** $H_T = 15\,\text{km}$, **(b)** $H_T = 20\,\text{km}$, **(c)** $H_T = 25\,\text{km}$, and **(d)** $H_T = 27\,\text{km}$. The displayed data originates from the same weather pattern (3), day (31$^{\text{st}}$ January 2022), and start time (14:00 UTC). We applied a lower ash concentration threshold of $0.2\,\text{mg}\,\text{m}^{-3}$ to define the edge of the cloud. The lines between data points are not model fits and are just used to guide the eye. The legend specifies the colour and data marker corresponding to each FL interval.

region (orange box in Figure 8) by approximately 50 to 150 FLs (Figure 8). The small fluctuations in time are likely to originate from vertical atmospheric turbulences. The light grey line indicates the average location of the maximum amount of mass, which decreases with time but remains, at least for the first 36 h, within the original release region. The 95% confidence interval (black dotted lines) of these data shows that there is very little variation in these results for different days (weather

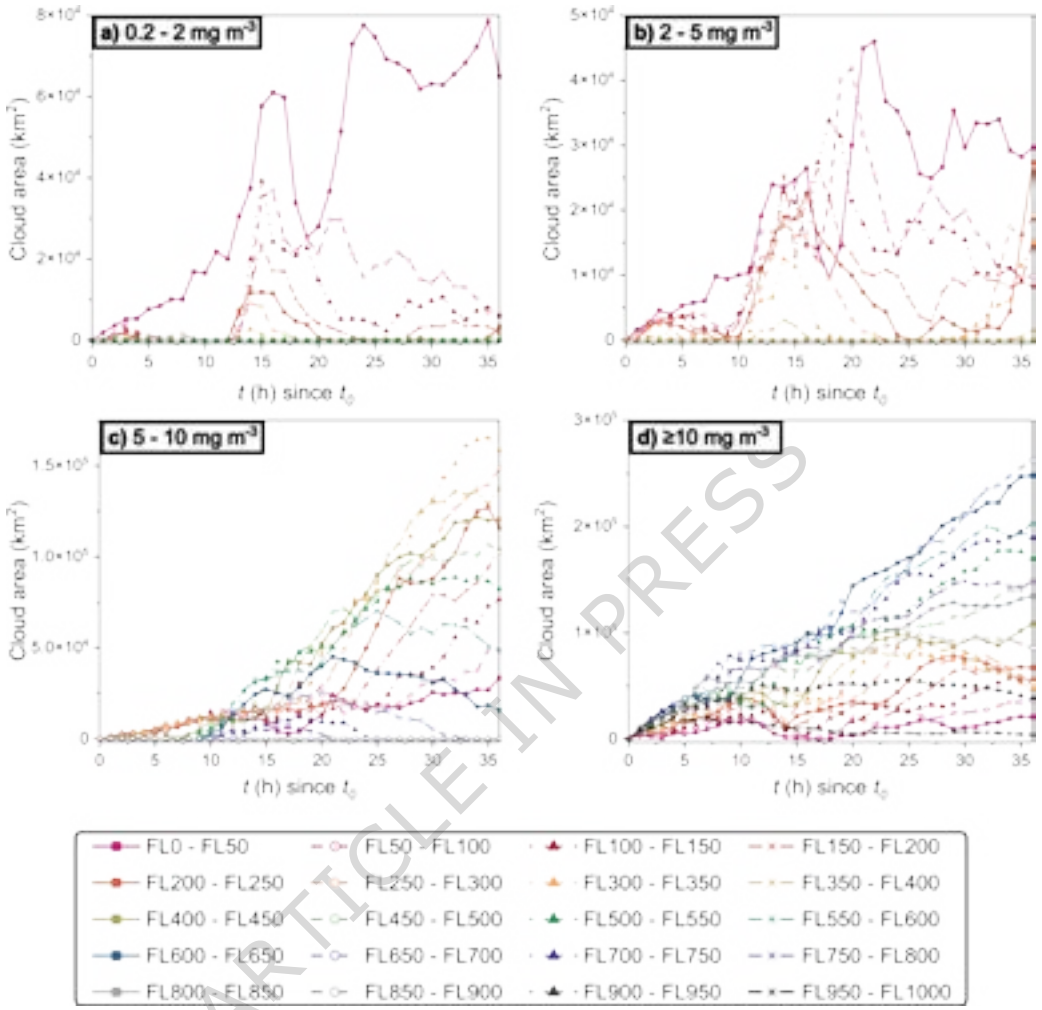

Figure 7: Ash cloud area within each 50 FL interval as a function of time for particle released at H_T = 27 km. The different subplots correspond to the different QVA thresholds **(a)** 0.2-2 mg m^{-3}, **(b)** 2-5 mg m^{-3}, **(c)** 5-10 mg m^{-3}, and **(d)** $\geq$ 10 mg m^{-3}. The data originate from the same day (31st January 2022) and start time (14:00 UTC). The lines between data points are not model fits and are just used to guide the eye. The y-axis varies in scale between the panels. The legend specifies the colour and data marker corresponding to each FL interval.

patterns) and start times.

We note that the computational domain of NAME in the vertical direction in our experiments is restricted to 30 km (approximately corresponding to FL1000). The maximum FL achieved for H_T = 27 km shown in Figure 8d reaches the top of the computational domain and it is therefore possible that some particles may be able to reach higher altitudes.

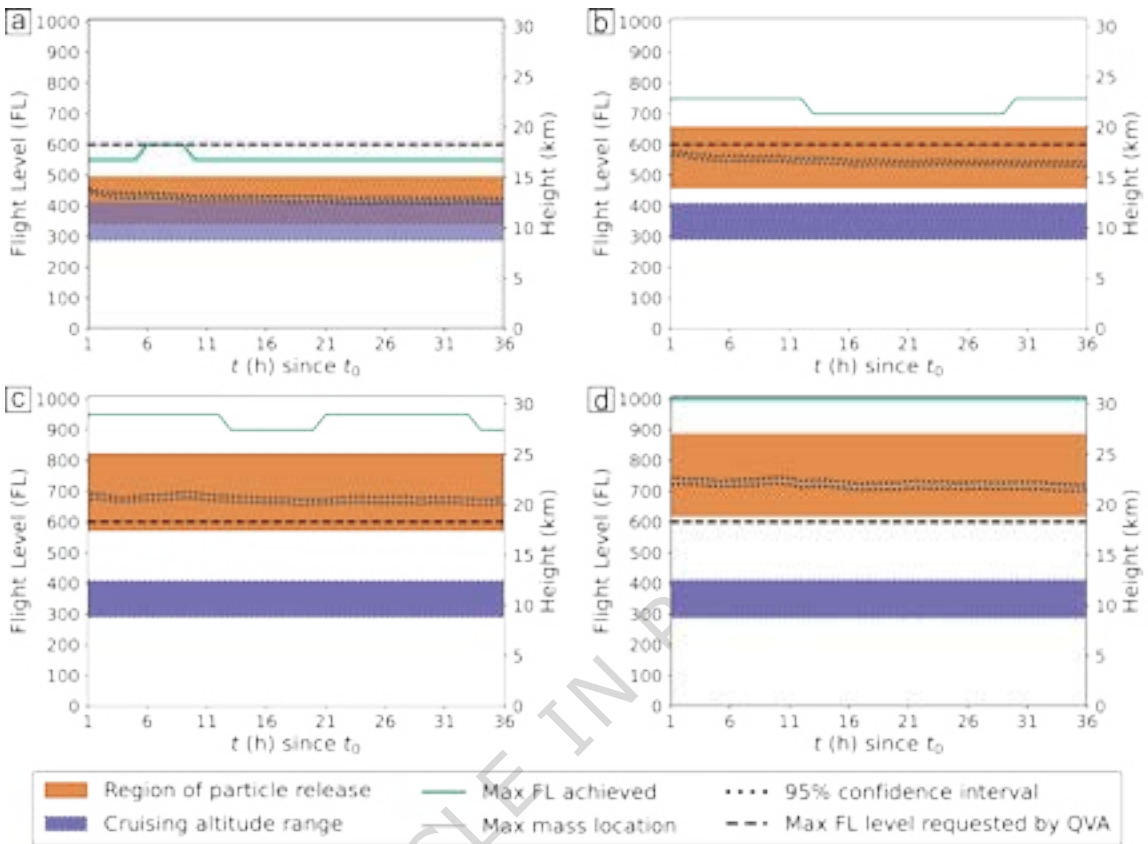

Figure 8: Maximum mass of particles in the atmosphere as a function of time for particle release heights of **(a)** $H_T = 15\,\text{km}$, **(b)** $H_T = 20\,\text{km}$, **(c)** $H_T = 25\,\text{km}$, and **(d)** $H_T = 27\,\text{km}$. The orange boxes correspond to the particle release regions, the purple boxes refer to the range of commercial aircraft cruising altitudes[53], ∼ FL290 to FL410. The green lines indicate the average maximum FL achieved by particles for all model runs. The light grey lines indicate the average FL location of the maximum mass, and the black dotted lines represent the 95% confidence interval, including all weather patterns, days, and release start times. The black dashed lines represent the maximum requested FL to be reported in QVA products.

Discussion

Our results and findings are a consequence of the unique ESPs for co-PDCs, and here, we discuss our results in the context of the aviation hazard. Firstly, we discuss the influence of weather pattern and release height. We found that the shape, size, or location characteristics of the co-PDC ash clouds cannot be related to a specific weather pattern. Even if the weather pattern is known, we also cannot predict the vertical cloud location (i.e., at a specific flight level). For a given weather pattern, the distance travelled by the ash cloud (up to 12 h) can also vary significantly. The only

generalisation that can be made is that weather patterns 5 to 8 (Figure 4e-h) result in less dispersed ash clouds, and remain closer to the source location over Iceland, relative to weather patterns 1 to 4 (Figure 4a-d). This means that, based on our current knowledge, robust statements and generalisations about how the location, area, or shape of an ash cloud from a co-PDC vary as a function of the weather pattern cannot be made. A model simulation using the specific weather data for the event is required to obtain the specific characteristics of the ash cloud shape, size, or location. Future work should compare our findings with the whole set of 30 weather patterns defined by Neal *et al.*[75]. Any generalisations linking dispersion and transport characteristics to weather patterns are more likely with a larger data set of weather patterns. For example, Harrison *et al.*[87] are able to identify mean, characteristic flow speeds in the mid-upper troposphere for each weather pattern when the full set of 30 is used. Here, in our case, we suggest that the relatively similar behaviour of ash clouds dispersed in weather patterns 5 to 8 (Figure 4e-h) originate from the grouping method, as together they only contain 9 of the 30 weather patterns, while weather patterns 1 to 4 (Figure 4a-d) contain 21 out of 30 weather patterns (Figure S1).

Previous work[57] has confirmed that the plume/release height is an extremely important eruption source parameter for modelling co-PDC ash dispersal, just like vent-derived eruptions[66,88]. Here, we have shown that changes in the ash concentration also depend on the H_T and associated MER, where only high (H_T=25 km & 27 km) release heights result in high ash concentrations (Figure 5c & d) in the first few hours since emission. As previously detailed, we modelled the co-PDC plumes as an ash release at a specific height range and not as a line source from the vent up to the plume top (as is done operationally by the London VAAC for standard vent-derived plumes). This impacts our observations as the particles are not released into the entire atmosphere but rather only into the stratosphere. The short t_r (10 min) is also of importance, as all the ash particles experience the same wind fields (including wind shear effects) and are therefore likely to remain in a similar location, with concentration changes largely due to different MERs, and total erupted mass.

For H_T = 25 km and H_T = 27 km, we observe very similar cloud behaviour in terms of location, shape, size, extent, and concentration (i.e., Figure 5). They are also similar in terms of the total cloud area distribution (i.e., Figure 6c & d). This is due to the high altitude in the stratosphere, where the particles are released. At these altitudes, less turbulence acts on the ash particles[89].

Our results highlight the importance of knowing H_T and any variations thereof during an ongoing eruption. For example, variation in a (vent-derived) H_T of 6 km by a 1 km uncertainty can impact the estimated minimum and maximum cloud area by a factor[62] of 3. Given the dispersion model output varies greatly with H_T and thus MER for both co-PDC plumes and vent-derived plumes[55,57,62,83,90,91], it would be beneficial to the forecasts and operational setups to know the exact release height from co-PDC plumes during a real-time event to initialise the dispersion modelling. This includes reconciling data and observations from different measurement methods such as visual ground-based observations, pictures or video footage, different remote sensing techniques (ground-

based radar, lidar, (visible) cameras, and satellites or aircraft observations) and potentially coupling them with numerical models[27,29,30,46,90–101]. Furthermore, these observations can be hindered by meteorological cloud coverage, adverse weather, differentiation between ash and ice or water, and night-time light limitations[18,27,29,102,103]. Finally, although the relationship between H_T and MER (Equation 5) has been shown to hold for large co-PDC events, the limits of this MER–H_T relationship remain to be tested for the full range of co-PDC plume heights.

The newly introduced QVA concentration thresholds help evaluate risk of volcanic ash encounters for the aviation industry. We have shown that the cloud extent with ash concentrations $\geq 0.2\,\mathrm{mg\,m^{-3}}$ increases with time (for at least the first 36 h). For short times after particle release, we observe high-concentrated ash clouds with small to non-existent areas of lower ash concentrations at the cloud margins (0.2-5 $\mathrm{mg\,m^{-3}}$; e.g., Figures 3–5). Across all our model runs, the maximum ash concentration achieved was $28\,840\,\mathrm{mg\,m^{-3}}$ (modelled for 3rd August 2017 at 1 h after particle release, $H_T = 27$ km at FL650 - FL700). However, similar high ash concentrations are observed throughout the whole dataset (often $\geq 10\,\mathrm{mg\,m^{-3}}$) and are thus a common feature of the co-PDC clouds modelled.

Previous work[33] has modelled the maximum ash concentration range generated from the 26th February 2000 eruption of Hekla, Iceland, along the flight path of a NASA DC-8 research aircraft that encountered ash on the 28th February 2000 and suffered engine damage[33,104]. The Hekla eruption column[33,105] with heights up to 12 km reached a maximum ash concentration of 4-5 $\mathrm{mg\,m^{-3}}$ on the flight path. Similarly, Witham *et al.*[33] modelled the ash concentrations during the 24th June 1982 eruption of Galunggung, Indonesia. An ash encounter with a British Airways Boeing 747 aircraft led to failure of all four engines[29,33] and the modelled concentrations reached a maximum of $\sim$ 45-320 $\mathrm{mg\,m^{-3}}$ for plume heights of 12-16 km, with large uncertainties given the uncertain eruption column height[33]. More broadly, the maximum ash concentration modelled by Witham *et al.*[33] for five different volcanic ash aircraft encounters is $200\,\mathrm{mg\,m^{-3}}$. For each simulation, they used a power law relationship between H_T and MER, which compares well with the Mastin[84] H_T-MER relationship. Furthermore, previous work[62] has analysed the ash concentration of the 2010 Eyjafjallajökull eruption on 6th May and found forecasted peak ash concentrations of $13\,\mathrm{mg\,m^{-3}}$ at FL000 - FL200. This is consistent with the $13\,\mathrm{mg\,m^{-3}}$ peak ash concentration found on 7th May by Beckett *et al.*[55] in FL000 - FL200 and FL200 - FL350 across different model parameter settings. For the determination of MER, both studies[55,62] used the Mastin[84]-H_T-MER relationship and applied a 5% distal fine ash fraction scaling, which accounts for physical processes such as aggregation and fall-out of large, heavy particles close to the source.

For our co-PDC clouds we found the maximum ash concentration to be $28\,840\,\mathrm{mg\,m^{-3}}$ located at FL650 - FL700 for $H_T = 27$ km, which corresponds to a MER of $2.4 \times 10^8\,\mathrm{kg\,s^{-1}}$. At FL300 - FL400 (corresponding to commercial airspace use), for the same model run and time since release start, the ash concentrations are $\leq 721\,\mathrm{mg\,m^{-3}}$. This concentration is in line with previous NAME studies of

ash-aircraft encounters from vent-derived plumes. However, the maximum ash concentrations found within our co-PDC clouds are extremely high relative to those previously reported for vent-derived plumes. This can be explained well by our different modelling approach, which reflects, at least in part, the different co-PDC source conditions. Firstly, we only released the particles in the top 30% of the plume (refer to Equation 4) to reflect transport and dispersion at a level of neutral buoyancy. Secondly, we used a fine TGSD appropriate for co-PDCs and have not applied a distal fine ash fraction scaling, meaning that the entire mass is applied to the downwind dispersion. Thirdly, we used higher H_T and thus MERs compared to these previous studies on vent-derived plumes.

We now consider the mass distribution within the ash cloud (Figure 8). After a short t_r (10 min), we track the mass of ash within the cloud as it moves downwind. Within the first 36 h, across all weather patterns, dates, and start times, we observe two consistent behaviours. (i) The maximum FL achieved remains 50 to 150 flight levels above the release region within the first 36 h. (ii) The elevation of maximum mass sits within the release region. The fine co-PDC grain size[15,18] contributes to this observation, as these particles have long atmospheric residence times and can travel far distances[18,27,38]. Particle sedimentation is still present, but the settling velocity is low compared to the vertical component of air velocity[106]. These findings are useful for future operational setups at VAACs that wish to consider the ash concentration from a co-PDC. The elevation of maximum mass is only expected to align with FLs used for commercial airspace when release heights are smaller than $H_T = 20$ km. However, as previously shown, the ash concentration remains high (relative to QVA) across most FLs (for release at $\geq H_T = 20$ km).

The different eruption start times provide both different weather conditions and boundary layer levels[76,77], but no extreme differences or patterns in the resulting ash cloud are observed. The focus on vertical atmospheric layers, e.g., flight levels, means that convective and vertical mixing needs to be considered, and the way these are modelled within NAME might have a minor impact on the vertical location, the particles achieve. Future work could continue to test these results by examining different release locations outside of Iceland and by further varying the meteorological impact. For example, previous observations at different latitudes found that the volcanic plume height attained is impacted by humidity and wind shear[96,107].

Our results also have potential implications for other dispersion events. In this study, we used the TGSD documented for the Campanian co-ignimbrite eruption[108]. This TGSD has a modal grain size of 37 µm and is likely to be representative of other co-PDC plumes[18], as all co-PDCs form by a common self-selecting process wherein segregated particles buoyantly lift off. However, this remains to be verified by further field and real-time investigations. Additionally, this work could be expanded and compared to other events that (re)suspend particulate matter in a similar way. This could include resuspended ash events[21,27,109–114], for example, as they show a similar grain size characteristics to co-PDCs[109,111]. Where the grain size modes of remobilised ash have been shown[111] to be 32-63 µm. Additionally, sub-Saharan dust[115–117] has a similar grain size[117] with a

mode 1-30 µm.

To conclude, here, we studied the vertical ash concentration, transport, and dispersion of co-PDC ash clouds from the ground surface (FL0) up to FL1000 ($\sim$ 30 km altitude) using eruption source parameters that are appropriate for (large) co-PDCs. We focused on large co-PDCs to provide an upper limit on the likely natural range. We showed that within our dataset the ash cloud location, shape, or size at each 50 flight levels cannot be directly related to a specific weather pattern, and thus these cloud characteristics cannot be pre-determined. We also observed 'very high' ash concentrations ($\geq 10\,\mathrm{mg\,m^{-3}}$) for all release/plume heights above $H_T = 20$ km. The ash clouds were observed to be compact in shape with little to no reduction in concentration towards the cloud margins. For all release heights under study ($H_T = 15$ km, 20 km, 25 km, & 27 km), variations in the ash concentration at each FL interval were observed. However, little variation in the associated cloud location is observed between the different FLs for a given plume height at 12 h after particle release. $H_T = 25$ km and $H_T = 27$ km generated clouds display a similar location and shape, due to the ash being released into the stratosphere. The total cloud area exceeding $0.2\,\mathrm{mg\,m^{-3}}$ at each 50 flight level interval increases with time (within the first 36 h) and hence increases the hazard to aviation. Again, within the first 36 h, the elevation of the maximum mass resides within the release region, and the maximum flight level achieved by the ash is 50 to 150 flight levels above the release region. Although the ash clouds generated from co-PDCs have a small total area (typically $< 300\,000\,\mathrm{km^2}$), they comprise very high ash concentrations (max. $28\,840\,\mathrm{mg\,m^{-3}}$) and thus, in the event of an eruption producing a co-PDC plume, could pose a significant hazard to aviation.

Declarations

Data availability

NAME III Version 8.6 was used in the transport and dispersion model simulations. The UK Met Office NAME model and UM output to drive NAME are available via license from the UK Met Office (©Crown Copyright, Met Office): https://www.metoffice.gov.uk/research/approach/modelling-systems/dispersion-model. The data-generating script used in this contribution can be found on Zenodo (Hagenbourger *et al.*[118]).

References

1. Burgisser, A., Peccia, A., Plank, T. & Moussallam, Y. Numerical simulations of the latest caldera-forming eruption of Okmok volcano, Alaska. en. *Bulletin of Volcanology* **86,** 77. ISSN: 1432-0819. doi:10.1007/s00445-024-01765-1 (2024).

2. Jones, T. J. *et al.* Physical properties of pyroclastic density currents: relevance, challenges and future directions. English. *Frontiers in Earth Science* **11.** ISSN: 2296-6463. doi:10.3389/feart.2023.1218645 (2023).

3. Dellino, P., Dioguardi, F., Isaia, R., Sulpizio, R. & Mele, D. The impact of pyroclastic density currents duration on humans: the case of the AD 79 eruption of Vesuvius. en. *Scientific Reports* **11,** 4959. ISSN: 2045-2322. doi:10.1038/s41598-021-84456-7 (2021).

4. Giordano, G. & Cas, R. A. F. Classification of ignimbrites and their eruptions. *Earth-Science Reviews* **220,** 103697. ISSN: 0012-8252. doi:10.1016/j.earscirev.2021.103697 (2021).

5. Lube, G., Breard, E. C. P., Esposti-Ongaro, T., Dufek, J. & Brand, B. Multiphase flow behaviour and hazard prediction of pyroclastic density currents. en. *Nature Reviews Earth & Environment* **1,** 348–365. ISSN: 2662-138X. doi:10.1038/s43017-020-0064-8 (2020).

6. Brown, R. J. & Andrews, G. D. M. in *The Encyclopedia of Volcanoes (Second Edition)* (ed Sigurdsson, H.) 631–648 (Academic Press, Amsterdam, 2015). ISBN: 978-0-12-385938-9. doi:10.1016/B978-0-12-385938-9.00036-5.

7. Dufek, J., Esposti Ongaro, T. & Roche, O. in *The Encyclopedia of Volcanoes (Second Edition)* (ed Sigurdsson, H.) 617–629 (Academic Press, Amsterdam, 2015). ISBN: 978-0-12-385938-9. doi:10.1016/B978-0-12-385938-9.00035-3.

8. Druitt, T. H. Pyroclastic density currents. *Geological Society, London, Special Publications* **145,** 145–182. doi:10.1144/GSL.SP.1996.145.01.08 (1998).

9. Sulpizio, R. *et al.* Predicting the block-and-ash flow inundation areas at Volcán de Colima (Colima, Mexico) based on the present day (February 2010) status. *Journal of Volcanology and Geothermal Research* **193,** 49–66. ISSN: 0377-0273. doi:10.1016/j.jvolgeores.2010.03.007 (2010).

10. Charbonnier, S. J. & Gertisser, R. Field observations and surface characteristics of pristine block-and-ash flow deposits from the 2006 eruption of Merapi Volcano, Java, Indonesia. *Journal of Volcanology and Geothermal Research. Volcanic Flows and Falls* **177,** 971–982. ISSN: 0377-0273. doi:10.1016/j.jvolgeores.2008.07.008 (2008).

11. Michol, K. A., Russell, J. K. & Andrews, G. D. M. Welded block and ash flow deposits from Mount Meager, British Columbia, Canada. *Journal of Volcanology and Geothermal Research* **169,** 121–144. ISSN: 0377-0273. doi:10.1016/j.jvolgeores.2007.08.010 (2008).

12. Bonadonna, C. *et al.* in *The Eruption of Soufrière Hills Volcano, Montserrat from 1995 to 1999* (eds Druitt, T. H. & Kokelaar, B. P.) 483–516 (Geological Society of London, 2002). ISBN: 978-1-86239-098-0. doi:10.1144/GSL.MEM.2002.021.01.22.

13. Ui, T., Matsuwo, N., Sumita, M. & Fujinawa, A. Generation of block and ash flows during the 1990–1995 eruption of Unzen Volcano, Japan. *Journal of Volcanology and Geothermal Research* **89,** 123–137. ISSN: 0377-0273. doi:10.1016/S0377-0273(98)00128-0 (1999).

14. Calder, E. S., Sparks, R. S. J. & Woods, A. W. Dynamics of co-ignimbrite plumes generated from pyroclastic flows of Mount St. Helens (7 August 1980). en. *Bulletin of Volcanology* **58,** 432–440. ISSN: 1432-0819. doi:10.1007/s004450050151 (1997).

15. Sigurdsson, H. & Carey, S. Plinian and co-ignimbrite tephra fall from the 1815 eruption of Tambora volcano. en. *Bulletin of Volcanology* **51,** 243–270. ISSN: 1432-0819. doi:10.1007/BF01073515 (1989).

16. Pistolesi, M. *et al. Tephra fallout and associated deposits* en. 2025.

17. Jones, T. J., Shetty, A., Chalk, C., Dufek, J. & Gonnermann, H. M. Identifying rheological regimes within pyroclastic density currents. en. *Nature Communications* **15,** 4401. ISSN: 2041-1723. doi:10.1038/s41467-024-48612-7 (2024).

18. Engwell, S. L. & Eychenne, J. in *Volcanic Ash* (eds Mackie, S., Cashman, K., Ricketts, H., Rust, A. & Watson, M.) 67–85 (Elsevier, 2016). ISBN: 978-0-08-100405-0. doi:10.1016/B978-0-08-100405-0.00007-0.

19. Andrews, B. J. & Manga, M. Effects of topography on pyroclastic density current runout and formation of coignimbrites. *Geology* **39,** 1099–1102. ISSN: 0091-7613. doi:10.1130/G32226.1 (2011).

20. Rosi, M. *et al.* A case history of paroxysmal explosion at Stromboli: Timing and dynamics of the April 5, 2003 event. *Earth and Planetary Science Letters* **243,** 594–606. ISSN: 0012-821X. doi:10.1016/j.epsl.2006.01.035 (2006).

21. Sparks, R. S. J. *et al. Volcanic plumes* eng. ISBN: 978-0-471-93901-6 (Wiley, Chichester, 1997).

22. Bursik, M. & Woods, A. W. The dynamics and thermodynamics of large ash flows. en. *Bulletin of Volcanology* **58,** 175–193. ISSN: 1432-0819. doi:10.1007/s004450050134 (1996).

23. Engwell, S. L., de'Michieli Vitturi, M., Esposti Ongaro, T. & Neri, A. Insights into the formation and dynamics of coignimbrite plumes from one-dimensional models. en. *Journal of Geophysical Research: Solid Earth* **121,** 4211–4231. ISSN: 2169-9356. doi:10.1002/2016JB012793 (2016).

24. Andrews, B. J. & Manga, M. Experimental study of turbulence, sedimentation, and coignimbrite mass partitioning in dilute pyroclastic density currents. *Journal of Volcanology and Geothermal Research* **225-226,** 30–44. ISSN: 0377-0273. doi:10.1016/j.jvolgeores.2012.02.011 (2012).

25. Woods, A. W. & Wohletz, K. Dimensions and dynamics of co-ignimbrite eruption columns. en. *Nature* **350,** 225–227. ISSN: 1476-4687. doi:10.1038/350225a0 (1991).

26. Wilson, T. M., Jenkins, S. & Stewart, C. in *Volcanic Hazards, Risks and Disasters* (eds Shroder, J. F. & Papale, P.) 47–86 (Elsevier, Boston, 2015). ISBN: 978-0-12-396453-3. doi:10.1016/B978-0-12-396453-3.00003-4.

27. Pardini, F. *et al.* Dynamics, Monitoring, and Forecasting of Tephra in the Atmosphere. en. *Reviews of Geophysics* **62,** e2023RG000808. ISSN: 1944-9208. doi:10.1029/2023RG000808 (2024).

28. Lechner, P., Tupper, A., Guffanti, M., Loughlin, S. & Casadevall, T. en. in *Observing the Volcano World: Volcano Crisis Communication* (eds Fearnley, C. J., Bird, D. K., Haynes, K., McGuire, W. J. & Jolly, G.) 51–64 (Springer International Publishing, Cham, 2018). ISBN: 978-3-319-44097-2. doi:10.1007/11157_2016_49.

29. Prata, F. & Rose, B. in *The Encyclopedia of Volcanoes (Second Edition)* (ed Sigurdsson, H.) 911–934 (Academic Press, Amsterdam, 2015). ISBN: 978-0-12-385938-9. doi:10.1016/B978-0-12-385938-9.00052-3.

30. Alexander, D. Volcanic ash in the atmosphere and risks for civil aviation: A study in European crisis management. en. *International Journal of Disaster Risk Science* **4,** 9–19. ISSN: 2192-6395. doi:10.1007/s13753-013-0003-0 (2013).

31. Folch, A., Costa, A. & Basart, S. Validation of the FALL3D ash dispersion model using observations of the 2010 Eyjafjallajökull volcanic ash clouds. *Atmospheric Environment. Volcanic ash over Europe during the eruption of Eyjafjallajöekull on Iceland, April-May 2010* **48,** 165–183. ISSN: 1352-2310. doi:10.1016/j.atmosenv.2011.06.072 (2012).

32. Webster, H. N. *et al.* Operational prediction of ash concentrations in the distal volcanic cloud from the 2010 Eyjafjallajökull eruption. en. *Journal of Geophysical Research: Atmospheres* **117.** ISSN: 2156-2202. doi:10.1029/2011JD016790 (2012).

33. Witham, C., Webster, H., Hort, M., Jones, A. & Thomson, D. Modelling concentrations of volcanic ash encountered by aircraft in past eruptions. *Atmospheric Environment. Volcanic ash over Europe during the eruption of Eyjafjallajöekull on Iceland, April-May 2010* **48,** 219–229. ISSN: 1352-2310. doi:10.1016/j.atmosenv.2011.06.073 (2012).

34. Guffanti, M., Casadevall, T. & Budding, K. Encounters of aircraft with volcanic ash clouds: A compilation of known incidents, 1953-2009. *U.S. Geol. Surv. Data Ser.* **545** (2011).

35. Casadevall, T. J., Delos Reyes, P. J. & Schneider, D. J. *The 1991 Pinatubo Eruptions and Their Effects on Aircraft Operations* tech. rep. (United States Geological Survey, 1999).

36. Miller, T. P. & Casadevall, T. J. eng. in *Encyclopedia of Volcanoes* (eds Sigurdsson, H., Houghton, B., Rymer, H., Stix, J. & McNutt, S.) 1st ed., 915–930 (Elsevier Science & Technology, Chantilly, 1999). ISBN: 978-0-12-643140-7.

37. Casadevall, T. J. *Volcanic hazards and aviation safety: lessons of the past decade.* tech. rep. (Flight safety foundation, flight safety digest, 1993).

38. Saxby, J., Beckett, F., Cashman, K., Rust, A. & Tennant, E. The impact of particle shape on fall velocity: Implications for volcanic ash dispersion modelling. en. *Journal of Volcanology and Geothermal Research* **362,** 32–48. ISSN: 03770273. doi:10.1016/j.jvolgeores.2018.08.006 (2018).

39. Kueppers, U. *et al.* The thermal stability of Eyjafjallajökull ash versus turbine ingestion test sands. en. *Journal of Applied Volcanology* **3,** 4. ISSN: 2191-5040. doi:10.1186/2191-5040-3-4 (2014).

40. Christmann, C., Nunes, R., Schmitt, A. & Guffanti, M. *Flying into Volcanic Ash Clouds: An Evaluation of Hazard Potential* in (STO, 2017). ISBN: ISBN 978-92-837-2112-3.

41. Müller, D. *et al.* Rheological and chemical interaction between volcanic ash and thermal barrier coatings. *Surface and Coatings Technology* **412,** 127049. ISSN: 0257-8972. doi:10.1016/j.surfcoat.2021.127049 (2021).

42. Wu, Y., Song, W., Dingwell, D. B. & Guo, H. Silicate ash-resistant novel thermal barrier coatings in gas turbines. *Corrosion Science* **194,** 109929. ISSN: 0010-938X. doi:10.1016/j.corsci.2021.109929 (2022).

43. Lokachari, S., Song, W., Yuan, J., Kaliwoda, M. & Dingwell, D. B. Influence of molten volcanic ash infiltration on the friability of APS thermal barrier coatings. *Ceramics International* **46,** 11364–11371. ISSN: 0272-8842. doi:10.1016/j.ceramint.2020.01.166 (2020).

44. Chen, W. R. & Zhao, L. R. Review – Volcanic Ash and its Influence on Aircraft Engine Components. *Procedia Engineering. 2014 Asia-Pacific International Symposium on Aerospace Technology, APISAT2014 September 24-26, 2014 Shanghai, China* **99,** 795–803. ISSN: 1877-7058. doi:10.1016/j.proeng.2014.12.604 (2015).

45. Bernard, A. & Rose, W. I. The injection of sulfuric acid aerosols in the stratosphere by the El Chichón volcano and its related hazards to the international air traffic. en. *Natural Hazards* **3,** 59–67. ISSN: 1573-0840. doi:10.1007/BF00144974 (1990).

46. Engwell, S. L. *et al.* Near-real-time volcanic cloud monitoring: insights into global explosive volcanic eruptive activity through analysis of Volcanic Ash Advisories. en. *Bulletin of Volcanology* **83,** 9. ISSN: 1432-0819. doi:10.1007/s00445-020-01419-y (2021).

47. ICAO Meteorology panel. *Quantitative Volcanic Ash (QVA) Concentration Information* tech. rep. (International civil aviation organization, 2023).

48. Saint, C., Beckett, F. M., Dioguardi, F., Kristiansen, N. & Tubbs, R. N. Using Simulated Radiances to Understand the Limitations of Satellite-Retrieved Volcanic Ash Data and the Implications for Volcanic Ash Cloud Forecasting. en. *Journal of Geophysical Research: Atmospheres* **129,** e2024JD041112. ISSN: 2169-8996. doi:10.1029/2024JD041112 (2024).

49. ICAO. *FOURTH MEETING OF THE INTERNATIONAL VOLCANIC ASH TASK FORCE (IVATF/4)* tech. rep. (International civil aviation organization, Montréal, Canada, 2012), 70 pp.

50. Prata, A. J. & Prata, A. T. Eyjafjallajökull volcanic ash concentrations determined using Spin Enhanced Visible and Infrared Imager measurements. en. *Journal of Geophysical Research: Atmospheres* **117.** ISSN: 2156-2202. doi:10.1029/2011JD016800 (2012).

51. ICAO. *Terrain clearance and vertical separation of aircraft (altimeter setting)* Circular 26-AN/23 (International civil aviation organization, Montreal, Canada, 1956).

52. ICAO. *MANUAL OF THE ICAO STANDARD ATMOSPHERE extended to 80 kilometers (262 500 feet)* tech. rep. Doc 7488/3, 3rd edition (International civil aviation organization, 1993).

53. Fichter, C., Marquart, S., Sausen, R. & Lee, D. S. The impact of cruise altitude on contrails and related radiative forcing. en. *Meteorologische Zeitschrift* **14,** 563–572. ISSN: 0941-2948. doi:10.1127/0941-2948/2005/0048 (2005).

54. Goblet, V., Fala, N. & Marais, K. *Identifying Phases of Flight in General Aviation Operations* en. in *15th AIAA Aviation Technology, Integration, and Operations Conference* (American Institute of Aeronautics and Astronautics, Dallas, TX, 2015). ISBN: 978-1-62410-369-8. doi:10.2514/6.2015-2851.

55. Beckett, F. M. *et al.* Atmospheric Dispersion Modelling at the London VAAC: A Review of Developments since the 2010 Eyjafjallajökull Volcano Ash Cloud. en. *Atmosphere* **11,** 352. ISSN: 2073-4433. doi:10.3390/atmos11040352 (2020).

56. Davies, T. *et al.* A new dynamical core for the Met Office's global and regional modelling of the atmosphere. en. *Quarterly Journal of the Royal Meteorological Society* **131,** 1759–1782. ISSN: 1477-870X. doi:10.1256/qj.04.101 (2005).

57. Hagenbourger, M., Beckett, F. M., Jones, T. J. & Engwell, S. L. Modeling the Transport and Dispersion of Volcanic Co-PDC Ash Clouds Using NAME: An Evaluation of Source Geometry and Mass Eruption Rate. en. *Journal of Geophysical Research: Atmospheres* **131,** e2025JD044031. ISSN: 2169-8996. doi:10.1029/2025JD044031 (2026).

58. Herzog, M. & Graf, H.-F. Applying the three-dimensional model ATHAM to volcanic plumes: Dynamic of large co-ignimbrite eruptions and associated injection heights for volcanic gases. en. *Geophysical Research Letters* **37,** L19807. ISSN: 1944-8007. doi:10.1029/2010GL044986 (2010).

59. Neri, A., Esposti Ongaro, T., Macedonio, G. & Gidaspow, D. Multiparticle simulation of collapsing volcanic columns and pyroclastic flow. en. *Journal of Geophysical Research: Solid Earth* **108,** 2202. ISSN: 2156-2202. doi:10.1029/2001JB000508 (2003).

60. Neri, A., Di Muro, A. & Rosi, M. Mass partition during collapsing and transitional columns by using numerical simulations. *Journal of Volcanology and Geothermal Research* **115,** 1–18. ISSN: 0377-0273. doi:10.1016/S0377-0273(01)00304-3 (2002).

61. Woods, A. W. & Kienle, J. The dynamics and thermodynamics of volcanic clouds: Theory and observations from the april 15 and april 21, 1990 eruptions of redoubt volcano, Alaska. *Journal of Volcanology and Geothermal Research. The 1989-1990 Eruptions of Redoubt Volcano, Alaska* **62,** 273–299. ISSN: 0377-0273. doi:10.1016/0377-0273(94)90037-X (1994).

62. Dioguardi, F., Beckett, F., Dürig, T. & Stevenson, J. A. The Impact of Eruption Source Parameter Uncertainties on Ash Dispersion Forecasts During Explosive Volcanic Eruptions. en. *Journal of Geophysical Research: Atmospheres* **125,** e2020JD032717. ISSN: 2169-8996. doi:10.1029/2020JD032717 (2020).

63. Andrews, B. J. Dispersal and air entrainment in unconfined dilute pyroclastic density currents. en. *Bulletin of Volcanology* **76,** 852. ISSN: 1432-0819. doi:10.1007/s00445-014-0852-4 (2014).

64. Oberhuber, J. M., Herzog, M., Graf, H.-F. & Schwanke, K. Volcanic plume simulation on large scales. *Journal of Volcanology and Geothermal Research* **87,** 29–53. ISSN: 0377-0273. doi:10.1016/S0377-0273(98)00099-7 (1998).

65. Jones, A., Thomson, D., Hort, M. & Devenish, B. *The U.K. Met office's next-generation atmospheric dispersion model, NAME III* in *Air Pollution Modeling and Its Application XVII* (eds Borrego, C. & Norman, A.-L.) (Springer US, Boston, MA, 2007), 580–589. ISBN: 978-0-387-68854-1.

66. Harvey, N. J. *et al.* Multi-level emulation of a volcanic ash transport and dispersion model to quantify sensitivity to uncertain parameters. English. *Natural Hazards and Earth System Sciences* **18,** 41–63. ISSN: 1561-8633. doi:10.5194/nhess-18-41-2018 (2018).

67. Dacre, H. F. *et al.* Evaluating the structure and magnitude of the ash plume during the initial phase of the 2010 Eyjafjallajökull eruption using lidar observations and NAME simulations. en. *Journal of Geophysical Research: Atmospheres* **116,** D00U03. ISSN: 2156-2202. doi:10.1029/2011JD015608 (2011).

68. Webster, H. & Thomson, D. Dry deposition modelling in a Lagrangian dispersion model. en. *International Journal of Environment and Pollution* **47,** 1. ISSN: 0957-4352, 1741-5101. doi:10.1504/IJEP.2011.047322 (2011).

69. Sparks, R. S. J., Moore, J. G. & Rice, C. J. The initial giant umbrella cloud of the May 18th, 1980, explosive eruption of Mount St. Helens. *Journal of Volcanology and Geothermal Research* **28,** 257–274. ISSN: 0377-0273. doi:10.1016/0377-0273(86)90026-0 (1986).

70. Mastin, L. G., Carey, S. N., Van Eaton, A. R., Eychenne, J. & Sparks, R. S. J. Understanding and modeling tephra transport: lessons learned from the 18 May 1980 eruption of Mount St. Helens. en. *Bulletin of Volcanology* **85,** 4. ISSN: 1432-0819. doi:10.1007/s00445-022-01613-0 (2022).

71. Van Eaton, A. R. *et al.* Volcanic lightning and plume behavior reveal evolving hazards during the April 2015 eruption of Calbuco volcano, Chile. en. *Geophysical Research Letters* **43,** 3563–3571. ISSN: 1944-8007. doi:10.1002/2016GL068076 (2016).

72. Meteorological Office. *Meteorological glossary* 6. ed. eng (ed Lewis, R. P. W.) ISBN: 978-0-11-400363-0 (H.M.S.O, London, 1991).

73. Walters, D. *et al.* The Met Office Unified Model Global Atmosphere 7.0/7.1 and JULES Global Land 7.0 configurations. English. *Geoscientific Model Development* **12,** 1909–1963. ISSN: 1991-959X. doi:10.5194/gmd-12-1909-2019 (2019).

74. Brown, A. *et al.* Unified Modeling and Prediction of Weather and Climate: A 25-Year Journey. EN. *Bulletin of the American Meteorological Society* **93,** 1865–1877. doi:10.1175/BAMS-D-12-00018.1 (2012).

75. Neal, R., Fereday, D., Crocker, R. & Comer, R. E. A flexible approach to defining weather patterns and their application in weather forecasting over Europe. en. *Meteorological Applications* **23,** 389–400. ISSN: 1469-8080. doi:10.1002/met.1563 (2016).

76. Dang, R., Yang, Y., Hu, X.-M., Wang, Z. & Zhang, S. A Review of Techniques for Diagnosing the Atmospheric Boundary Layer Height (ABLH) Using Aerosol Lidar Data. en. *Remote Sensing* **11,** 1590. ISSN: 2072-4292. doi:10.3390/rs11131590 (2019).

77. Dai, A. The diurnal cycle from observations and ERA5 in surface pressure, temperature, humidity, and winds. en. *Climate Dynamics* **61,** 2965–2990. ISSN: 1432-0894. doi:10.1007/s00382-023-06721-x (2023).

78. Bonadonna, C. & Phillips, J. C. Sedimentation from strong volcanic plumes. en. *Journal of Geophysical Research: Solid Earth* **108,** 2340. ISSN: 2156-2202. doi:10.1029/2002JB002034 (2003).

79. Carey, S. & Sparks, R. S. J. Quantitative models of the fallout and dispersal of tephra from volcanic eruption columns. en. *Bulletin of Volcanology* **48,** 109–125. ISSN: 1432-0819. doi:10.1007/BF01046546 (1986).

80. Sparks, R. S. J. The dimensions and dynamics of volcanic eruption columns. en. *Bulletin of Volcanology* **48,** 3–15. ISSN: 1432-0819. doi:10.1007/BF01073509 (1986).

81. Morton, B. R., Taylor, G. I. & Turner, J. S. Turbulent gravitational convection from maintained and instantaneous sources. en. *Proceedings of the Royal Society of London. Series A. Mathematical and Physical Sciences* **234,** 1–23. ISSN: 0080-4630, 2053-9169. doi:10.1098/rspa.1956.0011 (1956).

82. Global Volcanism Program. *Volcanoes of the World* 2024. doi:10.5479/si.GVP.VOTW5-2024.5.2.

83. Aubry, T. J. *et al.* New Insights Into the Relationship Between Mass Eruption Rate and Volcanic Column Height Based On the IVESPA Data Set. en. *Geophysical Research Letters* **50,** e2022GL102633. ISSN: 1944-8007. doi:10.1029/2022GL102633 (2023).

84. Mastin, L. G. *et al.* A multidisciplinary effort to assign realistic source parameters to models of volcanic ash-cloud transport and dispersion during eruptions. en. *Journal of Volcanology and Geothermal Research* **186,** 10–21. ISSN: 03770273. doi:10.1016/j.jvolgeores.2009.01.008 (2009).

85. Wilson, L., Sparks, R. S. J., Huang, T. C. & Watkins, N. D. The control of volcanic column heights by eruption energetics and dynamics. en. *Journal of Geophysical Research: Solid Earth* **83,** 1829–1836. ISSN: 2156-2202. doi:10.1029/JB083iB04p01829 (1978).

86. Newhall, C. G. & Self, S. The volcanic explosivity index (VEI) an estimate of explosive magnitude for historical volcanism. en. *Journal of Geophysical Research: Oceans* **87,** 1231–1238. ISSN: 2156-2202. doi:10.1029/JC087iC02p01231 (1982).

87. Harrison, S. R. *et al.* Identifying Weather Patterns Associated with Increased Volcanic Ash Risk within British Isles Airspace. *Weather and Forecasting* **37,** 1157–1168. ISSN: 0882-8156, 1520-0434. doi:10.1175/WAF-D-22-0023.1 (2022).

88. Devenish, B. J., Francis, P. N., Johnson, B. T., Sparks, R. S. J. & Thomson, D. J. Sensitivity analysis of dispersion modeling of volcanic ash from Eyjafjallajökull in May 2010. en. *Journal of Geophysical Research: Atmospheres* **117,** D00U21. ISSN: 2156-2202. doi:10.1029/2011JD016782 (2012).

89. Ko, H.-C., Chun, H.-Y., Geller, M. A. & Ingleby, B. Global Distributions of Atmospheric Turbulence Estimated Using Operational High Vertical-Resolution Radiosonde Data. *Bulletin of the American Meteorological Society* **105,** E2551–E2566. ISSN: 0003-0007, 1520-0477. doi:10.1175/BAMS-D-23-0193.1 (2024).

90. Mastin, L. G. *et al.* Progress in protecting air travel from volcanic ash clouds. en. *Bulletin of Volcanology* **84,** 9. ISSN: 0258-8900, 1432-0819. doi:10.1007/s00445-021-01511-x (2022).

91. Dürig, T. *et al.* REFIR- A multi-parameter system for near real-time estimates of plume-height and mass eruption rate during explosive eruptions. *Journal of Volcanology and Geothermal Research* **360,** 61–83. ISSN: 0377-0273. doi:10.1016/j.jvolgeores.2018.07.003 (2018).

92. Simionato, R. *et al.* Combining Visible- and Infrared-Wavelength Observations With Numerical Modeling to Describe Vulcanian Eruption Plumes at Sabancaya, Peru. en. *Journal of Geophysical Research: Solid Earth* **129,** e2024JB029326. ISSN: 2169-9356. doi:10.1029/2024JB029326 (2024).

93. Pelley, R. E. *et al.* A Near-Real-Time Method for Estimating Volcanic Ash Emissions Using Satellite Retrievals. en. *Atmosphere* **12,** 1573. ISSN: 2073-4433. doi:10.3390/atmos12121573 (2021).

94. Zidikheri, M. J., Lucas, C. & Potts, R. J. Estimation of optimal dispersion model source parameters using satellite detections of volcanic ash. en. *Journal of Geophysical Research: Atmospheres* **122,** 8207–8232. ISSN: 2169-8996. doi:10.1002/2017JD026676 (2017).

95. Corradini, S. *et al.* A Multi-Sensor Approach for Volcanic Ash Cloud Retrieval and Eruption Characterization: The 23 November 2013 Etna Lava Fountain. en. *Remote Sensing* **8,** 58. ISSN: 2072-4292. doi:10.3390/rs8010058 (2016).

96. Carey, S. N. & Bursik, M. in *The Encyclopedia of Volcanoes (Second Edition)* (ed Sigurdsson, H.) 571–585 (Academic Press, Amsterdam, 2015). ISBN: 978-0-12-385938-9. doi:10.1016/B978-0-12-385938-9.00032-8.

97. Scollo, S. *et al.* Eruption column height estimation of the 2011-2013 Etna lava fountains. *Annals of Geophysics* **57,** S0214. ISSN: 2037-416X, 1593-5213. doi:10.4401/ag-6396 (2014).

98. Wiegner, M. *et al.* Characterization of the Eyjafjallajökull ash-plume: Potential of lidar remote sensing. en. *Physics and Chemistry of the Earth, Parts A/B/C* **45-46,** 79–86. ISSN: 14747065. doi:10.1016/j.pce.2011.01.006 (2012).

99. Durant, A. J., Bonadonna, C. & Horwell, C. J. Atmospheric and Environmental Impacts of Volcanic Particulates. en. *Elements* **6,** 235–240. ISSN: 1811-5209, 1811-5217. doi:10.2113/gselements.6.4.235 (2010).

100. Prata, A. J. Satellite detection of hazardous volcanic clouds and the risk to global air traffic. en. *Natural Hazards* **51,** 303–324. ISSN: 1573-0840. doi:10.1007/s11069-008-9273-z (2009).

101. Rose, W. I., Bluth, G. J. S. & Ernst, G. G. J. Integrating retrievals of volcanic cloud characteristics from satellite remote sensors: a summary. en. *Philosophical Transactions of the Royal Society of London. Series A: Mathematical, Physical and Engineering Sciences* **358** (eds Francis, P., Neuberg, J. & Sparks, R. S. J.) 1585–1606. ISSN: 1364-503X, 1471-2962. doi:10.1098/rsta.2000.0605 (2000).

102. Hadley, D., Hufford, G. L. & Simpson, J. J. Resuspension of Relic Volcanic Ash and Dust from Katmai: Still an Aviation Hazard. EN. *Weather and Forecasting* **19,** 829–840. ISSN: 1520-0434, 0882-8156. doi:10.1175/1520-0434(2004)019<0829:RORVAA>2.0.CO;2 (2004).

103. Simpson, J. J. *et al.* The February 2001 Eruption of Mount Cleveland, Alaska: Case Study of an Aviation Hazard. en. *Weather and Forecasting* **17,** 691–704. ISSN: 0882-8156, 1520-0434. doi:10.1175/1520-0434(2002)017<0691:TFEOMC>2.0.CO;2 (2002).

104. Grindle, T. J. & Burcham, F. W. *Engine Damage to a NASA DC-8-72 Airplane from a High-altitude Encounter with a Diffuse Volcanic Ash Cloud* tech. rep. NASA/TM-2003-212030 (NASA, 2003).

105. Lacasse, C. *et al.* Weather radar observations of the Hekla 2000 eruption cloud, Iceland. *Bulletin of Volcanology* **66,** 457–473. doi:10.1007/s00445-003-0329-3 (2004).

106. McLean, D. *et al.* Opportunities to synchronise and date archaeological and climate records in Northwest Africa using volcanic ash (tephra) layers. en. *Libyan Studies* **55,** 48–68. ISSN: 0263-7189, 2052-6148. doi:10.1017/lis.2024.18 (2024).

107. Tupper, A., Textor, C., Herzog, M., Graf, H.-F. & Richards, M. S. Tall clouds from small eruptions: the sensitivity of eruption height and fine ash content to tropospheric instability. en. *Natural Hazards* **51,** 375–401. ISSN: 1573-0840. doi:10.1007/s11069-009-9433-9 (2009).

108. Marti, A., Folch, A., Costa, A. & Engwell, S. L. Reconstructing the plinian and co-ignimbrite sources of large volcanic eruptions: A novel approach for the Campanian Ignimbrite. en. *Scientific Reports* **6,** 21220. ISSN: 2045-2322. doi:10.1038/srep21220 (2016).

109. Del Bello, E. *et al.* Field-based measurements of volcanic ash resuspension by wind. *Earth and Planetary Science Letters* **554,** 116684. ISSN: 0012-821X. doi:10.1016/j.epsl.2020.116684 (2021).

110. Etyemezian, V. *et al.* Laboratory Experiments of Volcanic Ash Resuspension by Wind. *Journal of Geophysical Research: Atmospheres* **124,** 9534–9560. ISSN: 2169-897X. doi:10.1029/2018JD030076 (2019).

111. Liu, E. J. *et al.* Ash mists and brown snow: Remobilization of volcanic ash from recent Icelandic eruptions. en. *Journal of Geophysical Research: Atmospheres* **119,** 9463–9480. ISSN: 2169-8996. doi:10.1002/2014JD021598 (2014).

112. Leadbetter, S. J., Hort, M. C., von Löwis, S., Weber, K. & Witham, C. S. Modeling the resuspension of ash deposited during the eruption of Eyjafjallajökull in spring 2010. en. *Journal of Geophysical Research: Atmospheres* **117.** ISSN: 2156-2202. doi:10.1029/2011JD016802 (2012).

113. Thorsteinsson, T., Jóhannsson, T., Stohl, A. & Kristiansen, N. I. High levels of particulate matter in Iceland due to direct ash emissions by the Eyjafjallajökull eruption and resuspension of deposited ash. en. *Journal of Geophysical Research: Solid Earth* **117, B00C05.** ISSN: 2156-2202. doi:10.1029/2011JB008756 (2012).

114. Ernst, G. G. J., Sparks, R. S. J., Carey, S. N. & Bursik, M. I. Sedimentation from turbulent jets and plumes. en. *Journal of Geophysical Research: Solid Earth* **101,** 5575–5589. ISSN: 2156-2202. doi:10.1029/95JB01900 (1996).

115. Đorđević, D., Vukmirović, Z., Tošić, I. & Unkašević, M. Contribution of dust transport and resuspension to particulate matter levels in the Mediterranean atmosphere. *Atmospheric Environment* **38,** 3637–3645. ISSN: 1352-2310. doi:10.1016/j.atmosenv.2004.04.001 (2004).

116. Vukmirović, Z. *et al.* Analysis of the Saharan dust regional transport. *Meteorology and Atmospheric Physics* **85,** 265–273. doi:10.1007/s00703-003-0010-6 (2004).

117. Middleton, N. J. & Goudie, A. S. Saharan dust: sources and trajectories. *Transactions of the Institute of British Geographers* **26,** 165–181. ISSN: 0020-2754. doi:10.1111/1475-5661.00013 (2001).

118. Hagenbourger, M., Jones, T. J., Beckett, F. M. & Engwell, S. *Supporting Information: The ash concentration of co-PDC clouds: implications for operational modelling and the aviation hazard* 2025. doi:10.5281/zenodo.17611537.

Figure 1: Flight levels (FL) retain vertical separation despite atmospheric pressure variations due to different weather conditions and large changes in ground topography. The 'standard' region, shown in the middle of the figure, is shown as a reference. Despite the cruise flight level being fixed (e.g., FL 300), the aircraft changes its actual altitude (i.e., km above sea level) during flight.

Figure 2: The vertical resolution of the Met Office Unified Model (MetUM) compared with flight level, FL. **(a)** 'ρ' and 'θ' levels contain the wind vector data and the temperature data, respectively. The vertical resolution of both data sets decreases with increasing height above sea level (asl). **(b)** NAME outputs FL in steps of 50 in this study. Despite FL being pressure-based, the standard atmosphere pressure curve is used for comparison (1013.2 hPa $\equiv$ FL0). The purple dashed line indicates the maximum FL (FL600) requested by aviation for QVA analysis.

Figure 3: Illustration of the relationship between **(a)** the horizontal footprint of total column mass loadings ($\mathrm{g\,m^{-2}}$) and **(b-l)** the vertical output shown at selected flight levels (in $\mathrm{mg\,m^{-3}}$) at 12 h after the particle release. The black outline in (b - l) represents the boundary of total column mass loadings $\geq 0.2\,\mathrm{g\,m^{-2}}$. Particles were released at $H_T = 27$ km on 31$^{\mathrm{st}}$ Jan 2022 at 14:00 UTC. In all panels, a blue star indicates the release location. Note the difference in the range and the units of the colour bars between the total column (a) and vertical outputs b - l).

Figure 4: Ash cloud location displayed for the eight weather patterns at 12 h after particles were released at $H_T = 27$ km at 14:00 UTC. FL550 - FL600 is displayed for all. Each subfigure contains three separate NAME model outputs, and thus displays three different ash clouds generated for each weather pattern. These are indicated by the black arrows, and the dates correspond to the associated eruption/release start. Some of the ash clouds within a weather pattern slightly overlap in this figure. In all panels, a blue star indicates the release location, and the data are given as ash concentration in $\mathrm{mg\,m^{-3}}$.

Figure 5: Ash cloud locations for particle release heights of **(a)** $H_T = 15$ km, **(b)** $H_T = 20$ km, **(c)** $H_T = 25$ km, and **(d)** $H_T = 27$ km for weather pattern number 3 at 12 h since particle release start time. The particles were released on 31$^{\mathrm{st}}$ Jan 2022 at 14:00 UTC. Each subfigure shows three different model run outputs at FL300 - FL350 for different dates. In all panels, a blue star indicates the release location, and the data are given as ash concentration in $\mathrm{mg\,m^{-3}}$.

Figure 6: Total ash cloud area at each 50 FL as a function of time for particle release heights of **(a)** $H_T = 15$ km, **(b)** $H_T = 20$ km, **(c)** $H_T = 25$ km, and **(d)** $H_T = 27$ km. The displayed data originates from the same weather pattern (3), day (31$^{\mathrm{st}}$ January 2022), and start time (14:00 UTC). We applied a lower ash concentration threshold of $0.2\,\mathrm{mg\,m^{-3}}$ to define the edge of the cloud. The

lines between data points are not model fits and are just used to guide the eye. The legend specifies the colour and data marker corresponding to each FL interval.

Figure 7: Ash cloud area within each 50 FL interval as a function of time for particle released at $H_T = 27\,\text{km}$. The different subplots correspond to the different QVA thresholds **(a)** 0.2-2 $\text{mg}\,\text{m}^{-3}$, **(b)** 2-5 $\text{mg}\,\text{m}^{-3}$, **(c)** 5-10 $\text{mg}\,\text{m}^{-3}$, and **(d)** $\geq 10\,\text{mg}\,\text{m}^{-3}$. The data originate from the same day (31$^{\text{st}}$ January 2022) and start time (14:00 UTC). The lines between data points are not model fits and are just used to guide the eye. The y-axis varies in scale between the panels. The legend specifies the colour and data marker corresponding to each FL interval.

Figure 8: Maximum mass of particles in the atmosphere as a function of time for particle release heights of **(a)** $H_T = 15\,\text{km}$, **(b)** $H_T = 20\,\text{km}$, **(c)** $H_T = 25\,\text{km}$, and **(d)** $H_T = 27\,\text{km}$. The orange boxes correspond to the particle release regions, the purple boxes refer to the range of commercial aircraft cruising altitudes[53], $\sim$ FL290 to FL410. The green lines indicate the average maximum FL achieved by particles for all model runs. The light grey lines indicate the average FL location of the maximum mass, and the black dotted lines represent the 95% confidence interval, including all weather patterns, days, and release start times. The black dashed lines represent the maximum requested FL to be reported in QVA products.

Acknowledgements

The authors would like to acknowledge the Engineering & Physical Sciences Research Council (EPSRC), which funded this research (Grant reference EP/X525583/1). MH acknowledges funding support by the 'Stipendien für ein Masterstudium im Ausland' fellowship of the German Academic Exchange Service (DAAD). TJJ was also supported by a UK Research and Innovation (UKRI) Future Leaders Fellowship (Grant reference MR/W009781/1). SLE was supported by the NC-ODA grant NE/R000069/1: Geoscience for Sustainable Futures and publishes with permission of the CEO, British Geological Survey. We would like to acknowledge Sarah Millington and Julia Crummy from the Met Office and BGS, respectively, for their feedback on a manuscript draft.

Author contribution

MH and TJJ acquired the funding for this work. MH, TJJ and FMB designed the study. MH conducted the NAME model runs and data analysis with assistance from TJJ and FMB. SLE advised on co-PDC parameters and aviation-related topics. MH produced all tables and figures and wrote the initial draft manuscript that was edited by all co-authors.

Competing interests

The authors declare no competing financial or non-financial interests.

Ethics approval and consent to participate

Not applicable.